Energetic electron precipitation induced by oblique whistler mode chorus emissions

Yi-Kai Hsieh[1], Yoshiharu Omura[1], and Yuko Kubota[1]

[1]Research Institute for Sustainable Humanosphere, Kyoto University, Kyoto, Japan

Key Points:

- We performed test particle simulations for electrons in the radiation belt interacting with oblique chorus emissions in a 3D dipole field.
- Oblique chorus emissions cause more energetic electron precipitation than parallel chorus emissions.
- Combination of nonlinear trapping via Landau resonance and nonlinear scattering via cyclotron resonance causes higher precipitation rates.

Corresponding author: Yi-Kai Hsieh, yikai_hsieh@rish.kyoto-u.ac.jp

Abstract

Energetic electron accelerations and precipitations in the Earth's outer radiation belt are highly associated with wave-particle interactions between whistler mode chorus waves and electrons. We perform test particle simulation to investigate the electron behaviors interacting with both parallel and obliquely propagating chorus emissions at L=4.5. We build up a database of the Green's functions, which are treated as results of the input electrons interacting with one emission, for a large number of electrons interacting with whistler mode chorus emissions. The loss process of electron fluxes interacting with consecutive chorus emissions in the outer radiation belt are traced by applying the convolution integrals of distribution functions and the Green's functions. Oblique chorus emissions lead to more electron precipitation than that led by parallel chorus emissions. By checking the resonance condition and resonant energy at loss cone angle, we find that electrons are hardly dropped into the loss cone directly by Landau resonance. The nonlinear scattering via cyclotron resonance is the main process that pushes energetic electrons into the loss cone. We propose a 2-step precipitation process for oblique chorus emissions that contributes to more electron loss: (1) During the first chorus emission, the nonlinear trapping of Landau resonance moves an electron near the loss cone. (2) During the second emission, the nonlinear scattering of cyclotron resonance scatters the electron into the loss cone. The combination of Landau resonance by oblique chorus emissions and cyclotron resonance results in the higher precipitation rate than the single cyclotron resonance by purely parallel chorus emissions.

1 Introduction

Wave-particle interaction between whistler mode chorus emissions and electrons has been an important issue since it plays a significant role in the radiation belt dynamics. Whistler mode chorus emissions in the Earth's outer radiation belt are the main factors affecting the electron heating and pitch angle scattering(e.g., Summers et al., 1998; Thorne et al., 2005; Omura & Summers, 2006; Summers et al., 2007; Bortnik & Thorne, 2007; Millan & Baker, 2012). Chorus emissions are thought to scatter electrons of wide energy ranges into the loss cone (Horne & Thorne, 2003; Kennel & Petschek, 1966)

Microbursts of energetic electrons, which is a short-duration ($\leq$ 1 sec) and intense (tens of keV to a few MeV) electron precipitation, are often observed by balloons, rockets, and low Earth-orbiting satellites (e.g., Anderson & Milton, 1964; Rosenberg et al., 1990). The energetic electron precipitation (EEP) induced by chorus waves is the main cause of pulsating auroras (Nishimura et al., 2010; Miyoshi et al., 2015; Kasahara et al., 2018) and one of the processes removing energetic electrons from the Earth's outer radiation belt (e.g., R. Nakamura et al., 1995, 2000; Abel & Thorne, 1998). The EEP occurring with chorus events simultaneously or with some time delay at the same spatial region, namely the same magnetic local time and L-shell, are revealed by conjunctive satellite observations. Kersten et al. (2011) presented microbursts for >1 MeV electrons observed by SAMPEX and the associated simultaneous chorus waves detected by Solar Terrestrial Relations Observatory (STEREO) and Wind spacecraft. A chorus-driven relativistic electron microbursts event during the 8–9 October 2012 storm observed by SAMPEX and Van Allen Probes satellites is reported by Kurita et al. (2016). Breneman et al. (2017) presented a clear connection between chorus emissions and microburst detected by close conjunction observations of Van Allen Probes and FIREBIRD (Focused Investigations of Relativistic Electron Burst Intensity, Range, and Dynamics) II. Mozer et al. (2018) reported a chorus and microburst (>35 keV) event observed by Van Allen Probe-B at the inner magnetosphere and AC6-B satellite in the ionosphere, and verified that quasi-linear diffusion cannot explain the faster ($\sim$ 0.2 sec) microburst flux variations caused by large-amplitude chorus waves.

Several simulations provided direct evidence showing the chorus-driven EEP. Rosenberg et al. (1990) applied simple test particle simulations showing direct precipitation and mirrored precipitation of 20–100 keV electrons induced by chorus waves. Hikishima et al. (2010) performed a self-consistent full-particle simulation showing a one-to-one correspondence between microbursts of electrons at 10–100 keV and chorus emissions. Saito et al. (2012) reported that microbursts of relativistic electrons (MeV) of the outer belt are caused by chorus wave-particle interactions at high latitudes by performing three-dimensional test particle simulations and time-of-flight analysis (Miyoshi et al., 2010). Recently, Chen et al. (2020) presented a model of microbursts induced by ducted chorus waves showing bouncing chorus packets and the corresponding electron precipitation at hundreds of keV. Nevertheless, the above simulations are all under the parallel propagating assumption. Not only parallel but also oblique chorus emissions are usually observed in the inner magnetosphere (e.g., Santolík et al., 2009; Mourenas et al., 2015). Oblique whistler mode wave-particle interactions accelerate electrons and lower their equatorial pitch angles via Landau resonance efficiently (Hsieh & Omura, 2017a, 2017b). Based on this phenomenon, the Landau resonance should contribute to precipitation of 10–100 keV electrons or even relativistic electrons. The relation between chorus driven EEP and the Landau resonance has not been clarified yet.

In this study, we present a comprehensive analysis of electron acceleration and precipitation in the outer radiation belt induced by oblique whistler mode chorus emissions. We build three Green's function sets for electrons from 10 keV to 6 MeV by demonstrating three-dimensional test particle simulations at L=4.5 for three different wave models with different wave normal angles. The evolution of electron fluxes caused by repeated chorus emissions is reproduced by applying convolution integrals of electron distribution functions and the Green's function sets. We compare the energetic electron precipitation rates for different longitudinal wave generation regions and different wave normal angles.

The structure of this paper is as follows. In Section 2 we explain our simulation method and describe the possible loss processes by showing trajectories of resonant electrons. Results of convolution integrals are shown in Section 3. In Section 3.1 we compare results of different longitudinal chorus generation ranges and different wave normal angles for electrons initially at 10–30 keV. In Section 3.2 we check how fast high equatorial pitch angle electrons precipitate into the loss cone. The resonance conditions for cyclotron, Landau, and higher-order cyclotron resonances are discussed in Section 4. We also propose a two-step precipitation process, which does not occur in purely parallel chorus wave-particle interactions, due to combination of Landau resonance and cyclotron resonance in Section 4. Finally, the summary is shown in Section 5.

2 Test Particle Simulation & Green's functions

We apply test particle simulations to reproduce wave-particle interactions between whistler mode chorus emissions and electrons in the outer radiation belt. We simulate the wave-particle interactions around $L = 4.5$ in a three-dimensional dipole field, and the electron plasma frequency to cyclotron frequency ratio is set to be a constant ω_{pe}/Ω_{e0} =4, where ω_{pe} is electron plasma frequency and Ω_{e0} is the equatorial electron cyclotron frequency. Three different whistler mode wave models are used in the test particle simulations. Generally, all the wave models are generated at the equator and propagate both northward and southward with rising tone frequencies $\omega = 0.25$–$0.5\Omega_{e0}$ with subpacket structures. The frequency and amplitude variations follow the chorus equations, i.e., equations (106) and (107) of Omura (2021). Within $|Lat| \leq 2^\circ$, where Lat is magnetic latitude, the waves perform parallel propagating along with convective growth (Omura et al., 2008, 2009). The background parameters and equations of wave propagation within $|Lat| \leq 2^\circ$ in this study follow the settings in Hsieh et al. (2020). The equatorial wave amplitude and wave frequency are the same as shown in Figure 1 of Hsieh et al. (2020).

Table 1. Parameters used in simulations

Parameters		Normalized value	Real value
L-shell	L		4.5
Equatorial background magnetic field	B_{0eq}		342 nT
Equatorial electron gyrofrequency	Ω_{e0}		9.48 kHz
Electron plasma frequency	ω_{pe}	$4\ \Omega_{e0}$	37.9 kHz
Cold electron density	n_e		18/cc
Source electron density	n_h	$0.005\ n_e$	0.09/cc
Wave frequency	ω	$0.25 - 0.5\ \Omega_{e0}$	$2.37 - 4.74$ kHz
Parallel thermal velocity of source electrons	$V_{t\parallel}$	0.15 c	45,000 km/s
Averaged perpendicular velocity of source electrons	$V_{\perp 0}$	0.3 c	90,000 km/s
Charge to mass ratio	q/m_0	$-1e/m_e$	-1.76×10^{11} C/kg
Equivalent number of particles for a delta function	N_p		3,600

Wave phases across each subpacket may not be continuous, which means that when a subpacket generates at the equator its wave phase is not connected to the previous subpacket. Hiraga and Omura (2020) prove that the phase discontinuity does not affect the trapping rate. Thereby, we simply apply continuous wave phase for subpackets in our wave models.

In Case 1, we assume purely parallel propagating chorus emissions, and in Case 2 and Case 3 we apply oblique propagating chorus emissions. At $2^\circ < |Lat| < 45^\circ$, wave normal angles θ are linear functions of Lat. At $|Lat| \leq 45^\circ$, wave normal angles θ are a constant θ_{max}. The maximum wave normal angles θ_{max} are 20° and 60° for Case 2 and Case 3, respectively. According to the ray-tracing result (Yamaguchi et al., 2013), we assume that all wave normals point outward and lie on a meridian plane. Parameters assumed in simulations are listed in Table 1. We follow the configuration of the wave field explained in Appendix B of Hsieh and Omura (2017a). Conversion of wave components in the field-aligned coordinates to the Cartesian coordinates is described later in Appendix A. In the present study, the relativistic equations of motion of electrons are numerically solved by the Bumeman-Boris method.

2.1 Analyses of pitch angle scatterings

We examine the results of the test particle simulations and deduce the behavior of pitch angle scatterings. Figure 1 shows 4 examples for electrons starting at kinetic energy $K = 50$ keV and equatorial pitch angle $\alpha = 20^\circ$ in Case 3. Figure 1a plots electron trajectories in a Lat–$v_\parallel$ (latitude–electron parallel velocity) phase space. The red and blue curves represent resonance velocities of $n = 1$ cyclotron resonance and $n = 0$ Landau resonance, respectively. The resonance velocities are given by

$$V_R = \frac{1}{k_\parallel}\left(\omega - \frac{n\Omega_e}{\gamma}\right), \tag{1}$$

where n is the harmonic number, $k_\parallel$ is the parallel wave number, Ω_e is local electron cyclotron frequency, and γ is the Lorentz factor. The dotted lines stand for $\omega = 0.25\Omega_{e0}$ and the dashed lines denote $\omega = 0.5\Omega_{e0}$. Note that electrons interact with chorus emissions when moving with the parallel velocity $v_\parallel$ close to V_R. Hence, we can recognize that an electron is affected by a certain resonance in Figure 1a. Figure 1b shows electron trajectories and spatiotemporal profile of generation and propagation of chorus wave amplitude. We can read the timing of electrons undergoing resonances and make sure the electrons are inside the wave subpackets in Figure 1b. In Figures 1a and 1b, the solid

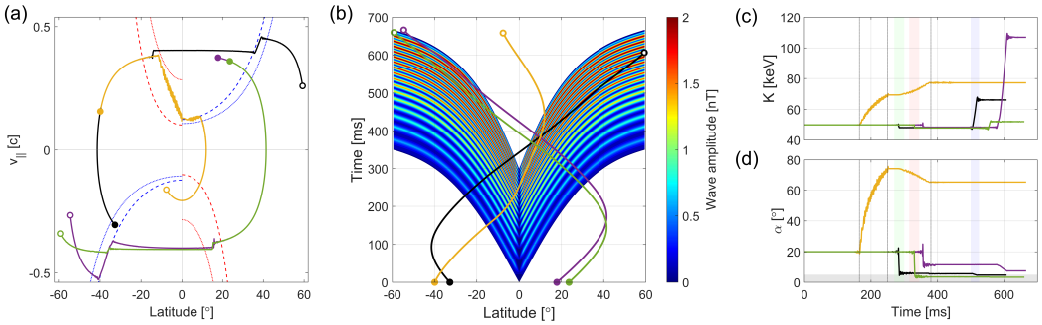

Figure 1. Examples for electrons interacting with a pair of oblique chorus emissions. The electrons initially have the same energy and equatorial pitch angle at different positions along the magnetic field line. The solid and hollow circles indicated the beginning and ending if each trajectories, respectively. (a) Electron trajectories in a *Lat*-$v_{||}$ phase space. (b) Electron trajectories and spatiotemporal profile of generation and propagation of chorus wave amplitude for Case 3 with subpacket structure. (c) Time series of kinetic energy variations. (d) Time series of equatorial pitch angle variations.

and hollow circles indicated the beginning and ending if each trajectories, respectively. There are two main processes in the whistler mode wave-particle interactions. One is the nonlinear scattering process, which makes electron energy slightly smaller and lowers the α of the electron. The other is the nonlinear trapping process, which causes effective energy gain of the resonant electrons. Figure 1c shows the time series of kinetic energies, which helps us to verify the resonance processes. Figure 1d denotes the time series of equatorial pitch angles α. Notice that our target L value is 4.5, so the related equatorial loss cone angle α_{loss} is 4.56° corresponding to an altitude of 100 km from the Earth's surface. The green curve drops to the loss cone, which is shown as the gray area, around time=320 ms (red area). This electron undergoes nonlinear scattering of $n = 1$ cyclotron resonance. Most of the precipitated electrons undergo this process. The yellow curve undergoes two nonlinear trapping processes. The first one is the $n = 1$ cyclotron resonance ($\sim$ 165–250 ms) and the second one is the $n = 0$ Landau resonance ($\sim$ 250–380 ms). Both resonances make effective accelerations but the different tendencies of pitch angle scattering. The first one makes higher α and the second one leads to lower α. The black curve is also affected by 2 resonances. Around 280 ms (green area) the electron drops close to the loss cone by nonlinear scattering of the $n = 1$ cyclotron resonance, and then at around 500 ms (blue area) it is pushed into the loss cone by the nonlinear trapping of the $n = 0$ Landau resonance. Here we find that Landau resonance can directly cause electron precipitation. However, this kind of precipitation by Landau resonance is rare and it requires an electron already close to the loss cone. The purple curve first undergoes $n = 1$ nonlinear scattering process and then undergoes a significant $n = 0$ nonlinear trapping. Nonetheless, the nonlinear trapping via the $n = 0$ Landau resonance is not able to scatter the electron into the loss cone. By checking the electron trajectories, we find that:

1. Most cases of EEP are directly caused by nonlinear scattering of the $n = 1$ cyclotron resonance.
2. Nonlinear trapping by the $n = 0$ Landau resonance also directly contributes to EEP, but the opportunity is much less than the above one.

2.2 Green's function method

Based on the result of the test particle simulations, we build numerical Green's function sets and employ the Green's function method and convolution integral (Omura et al., 2015; Kubota & Omura, 2018) to demonstrate the evolution of electron fluxes in the outer radiation belt. A Green's function $G(K, K_0, \alpha, \alpha_0)$ is treated as a result of one cycle of chorus wave-particle interactions with respect to a given initial distribution function $\delta(K-K_0, \alpha-\alpha_0)$, where δ is the Dirac delta function, K_0 is the initial kinetic energy, and α_0 is the initial equatorial pitch angle. We build up a set of Green's functions for electron K ranges from 10 keV to 6 MeV with an interval 10 keV, and α ranges from 5° to 89° with an interval 1°. The input electrons in the test particle simulations have random numbers in kinetic energy (10 keV $\leq K \leq$ 6 MeV), equatorial pitch angle ($5° \leq \alpha \leq 89°$), gyrophases $0 \leq \phi < 2\pi$, and locations within 2 mirror points. The equivalent number of electrons for a Green's function is $3,600$. Thereby, in total $183,600,000$ input electrons are used to generate one Green's function set. After the test particle simulations, we calculate the Green's functions from the results following the method introduced in Kubota and Omura (2018).

3 Results of convolution integrals

Tsurutani et al. (2009) suggested that 10–100 keV electrons may keep undergoing cyclotron resonance with parallel chorus subpackets for several wave cycles and be transported into the loss cone rapidly. Then, the rapid pitch angle transport rate is reported by (Lakhina et al., 2010) by calculating wave-particle diffusion coefficient. Therefore, the EEP process may not occur within only single chorus packet.

To reproduce the wave-particle interactions for consecutive chorus emissions, the first step is to set an initial electron distribution function and then obtain a new distribution function by applying a Green's function set. The second step is to regard the new distribution function as a new initial distribution function, and then apply the Green's functions again for the next distribution function. By repeating the steps m times, we can simulate the results of wave-particle interactions of m successive emissions without calculating the test particle simulation for m emissions, whose simulation costs a lot of computation resources. This process is called convolution integral (Omura et al., 2015). Considering the chorus emission generation localized in longitude (e.g., W. Li et al., 2009; Meredith et al., 2003) and electron drift motions, the equation of convolution integral after m cycles of interaction is given by (Kubota & Omura, 2018)

$$f_m(K, \alpha, \Phi_w) = \sum_{\alpha_j} \sum_{K_i} \sum_{\Phi_w} f_{m-1}(K_j, \alpha_i, \Phi_w) G^{\Phi}(K, K_i, \alpha, \alpha_j, \Phi - \Phi_w) \Delta\Phi \Delta K_i \Delta\alpha_j \quad (2)$$

$$+ \sum_{\bar{\Phi}_w} f_{m-1}(K, \alpha, \bar{\Phi}_w) G_0^{\Phi}(K, \alpha, \Phi - \bar{\Phi}_w) \Delta\Phi \,, \quad (3)$$

where f_m means the bounce-averaged distribution function after m-cycle interaction, and Φ_w and $\bar{\Phi}_w$ mean the longitudinal position inside and outside the chorus generation region, respectively. Since the duration of a chorus emission is much shorter than the time scale of electron drift motion, the drift degrees of an electron are very small during one-cycle interaction. Thereby, we assume that an electron does not drift into or out of the chorus generation region during one-cycle interaction when computing convolution integrals. Since the loss cone angle $\alpha_{loss} = 4.56°$, we treat the flux at $\alpha < 5°$ as electron precipitate into the Earth's atmosphere. In the convolution integral, the loss part of f_m will not participate in the calculation for f_{m+1}.

3.1 Uniform initial distribution function at 10–30 keV

3.1.1 Comparison among different generation ranges

We set an initial electron equatorial distribution function F^{Φ}_{0EQ} as a stationary distribution function with uniform K from 10 to 30 keV and uniform α from 5° to 89°. The relation between equatorial distribution function F^{Φ}_{mEQ} and the bounce-averaged distribution function f_m is

$$F^{\Phi}_{mEQ} = f_m(K, \alpha, \Phi)A(K, \alpha, h = 0) \ . \tag{4}$$

The A is a parameter concerning the phase space volume of trapped electrons given by

$$A(E, \alpha, h) = 2\pi m_0^{3/2} K^{1/2} \left(1 + \frac{K}{m_0 c^2}\right) \left(2 + \frac{K}{m_0 c^2}\right)^{1/2} \left[1 - \frac{B_0(h)}{B_{mp}(\alpha)}\right]^{-1/2} \sin 2\alpha \ , \tag{5}$$

where $B_0(h)$ is the background magnetic field at distance along the field line from the equator h, $B_{mp}(\alpha)$ is the background magnetic field at the mirror point for an electron with an equatorial pitch angle α, m_0 is electron rest mass, and c is light speed. The initial distribution is treated as source electrons generating the waves. We also assume an incessant influx of source electrons from the Earth's tail into the inner magnetosphere. Thereby, we keep the F^{Φ}_{0EQ} as a constant distribution during all cycles of chorus interactions. We show three different chorus generation regions: $\Delta\Phi_w$ = (1) 10°, (2) 60°, and (3) 90°. Note that the total initial flux and the influx integrated over E, α, and Φ are normalized to $1m^{-2}$. We apply the convolution integral method described above to the initial distribution function.

Figure 2 shows the equatorial distribution functions F^{Φ}_{mEQ} integrated over the longitudinal direction with interaction cycle m = (a) 20, (b) 50, (c) 600, and (d)1000 for Case 3 ($\theta_{max} = 60°$). It is natural that wider $\Delta\Phi_w$ results in more effective electron acceleration. After 1000 cycles of interaction, electron flux with $\Delta\Phi_w = 90°$ reaches more than 5 MeV. On the other hand, the maximum K in $\Delta\Phi_w = 10°$ case is about 4 MeV. The corresponding cross-sections are shown in Figure 3. From $\Phi = 0°$ to the white dashed lines are the range of longitudinal wave generation area. Figure 3c shows that some electrons can undergo the second acceleration process after 600 or more cycles of interaction, and also demonstrates that the wider $\Delta\Phi_w$ gives electrons more opportunity for wave-particle interactions. The precipitation rate ΔN_L (solid lines) and total electron fluxes N_{total} (dotted lines) are plotted in Figures 4a–c for $\Delta\Phi_w = 10°, 60°$, and 90°, respectively. The purple, blue, green, and red curves respectively denote $m = 20, 50, 600,$ and 1000. The ΔN_L is given by

$$\Delta N_L = \sum_{\Phi} \sum_{\alpha_L} f_m(K, \alpha_L, \Phi)\tilde{A}(K, \alpha_L)\Delta\alpha R_{EQ}\Delta\Phi \ , \tag{6}$$

where α_L is the equatorial pitch angles corresponding to the precipitated electrons, and $\tilde{A}$ is obtained by integrating A over the distance h along the magnetic field line between the two mirror points $-h_m$ and $+h_m$.

$$\tilde{A} = \int_{-h_m}^{+h_m} A(E, \alpha, h)dh \ . \tag{7}$$

The N_{total} is expressed as

$$N_{total} = \sum_{\Phi} \sum_{\alpha} f_m(K, \alpha, \Phi)\tilde{A}(K, \alpha)\Delta\alpha R_{EQ}\Delta\Phi \ . \tag{8}$$

It is obvious that after more interaction cycles, both electron precipitation and acceleration increased. We can find MeV electron precipitation at the early stage ($m = 20$) for Figures 4a–c. In Figures 4b and 4c, we find precipitation greater than 4 MeV.

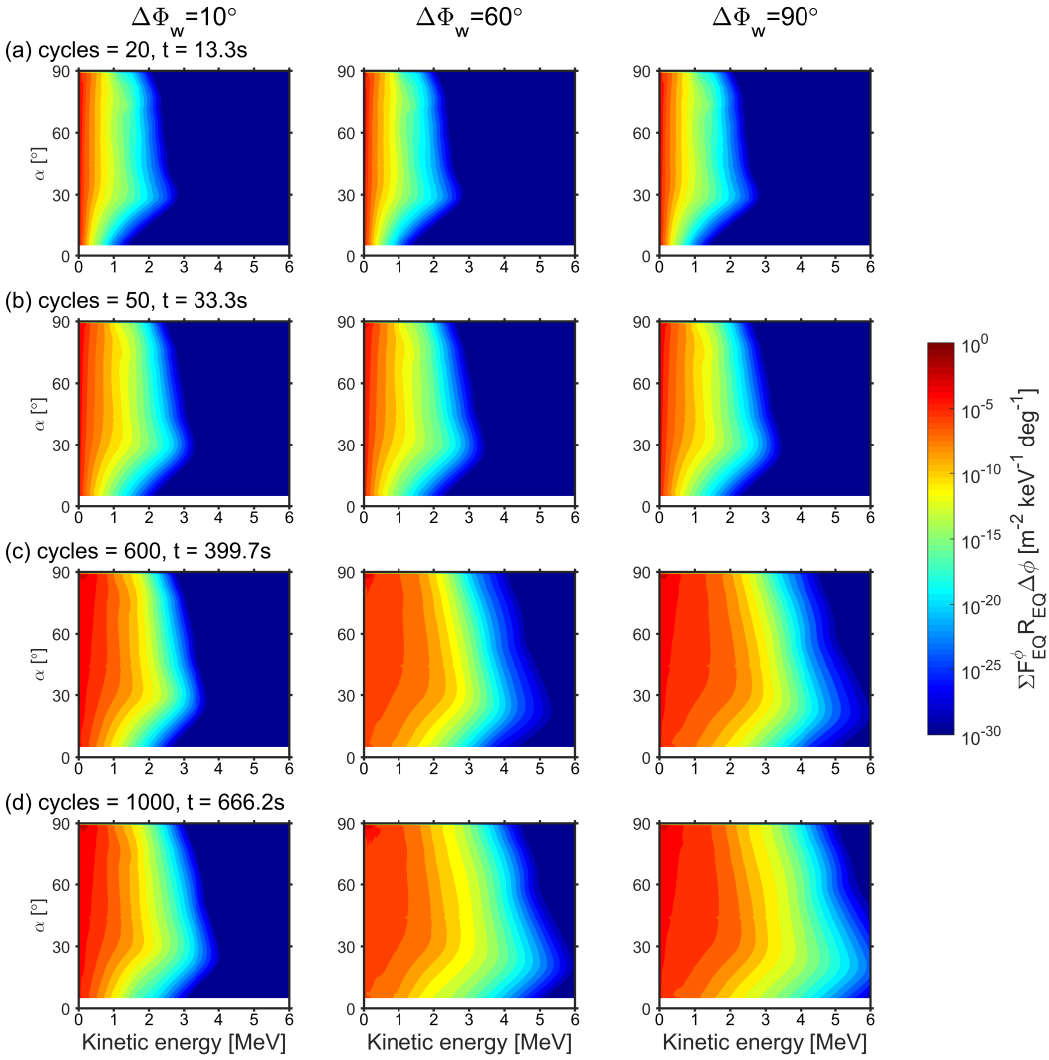

Figure 2. (a–d) Time evolution of the equatorial electron distribution functions $F^{\Phi}_{mEQ}(E, \alpha, \Phi)$ summed over the longitudinal direction as functions of kinetic energy K and equatorial pitch angle α for Case 3 (θ_{max}=60°). The chorus emissions exist in longitudinal ranges (left column) $\Delta\Phi = 10°$, (middle column) $\Delta\Phi = 60°$, and (right column) $\Delta\Phi$=90°. The initial equatorial distribution function $F^{\Phi}_{0EQ}(E, \alpha, \Phi)$ is set as a static distribution of which energy ranges from 10 to 30 keV, equatorial pitch angle ranges from 5° to 89°, and longitudinal ranges from 0° to (left column) 10°, (middle column) 60°, and (right column) 90°. These integrations of F^{Φ}_{0EQ} over E, α, and the longitude are normalized to $1m^{-2}$.

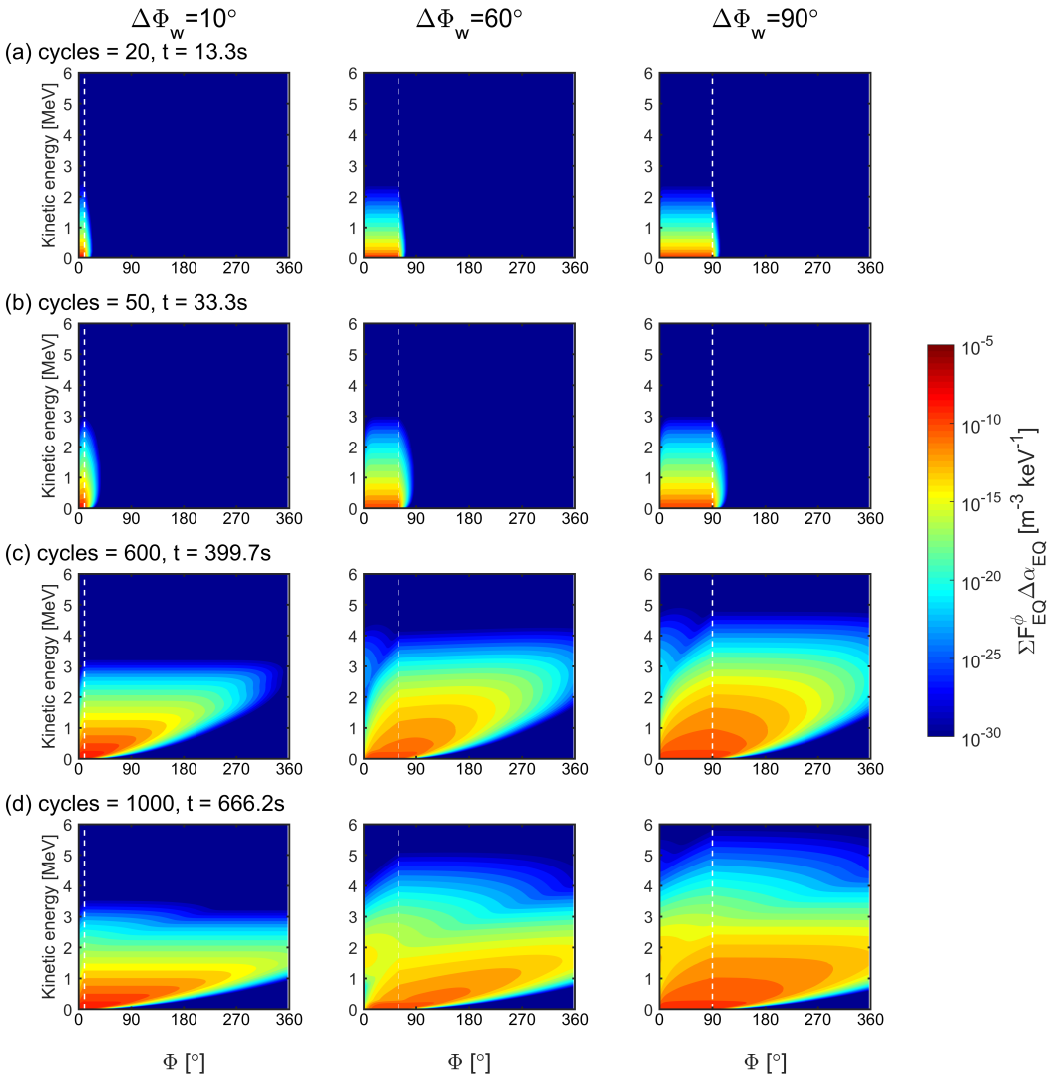

Figure 3. (a–d) Time evolution of the equatorial electron distribution functions $F^{\Phi}_{mEQ}(E, \alpha, \Phi)$ summed over the equatorial pitch angle α from 5° to 89° as functions of longitudinal angle Φ and kinetic energy K for Case 3 (θ_{max}=60°). The chorus emissions exist in longitudinal ranges (left column) $\Delta\Phi_w = 10°$, (middle column) $\Delta\Phi_w = 60°$, and (right column) $\Delta\Phi_w$=90° as shown by white dashed lines.

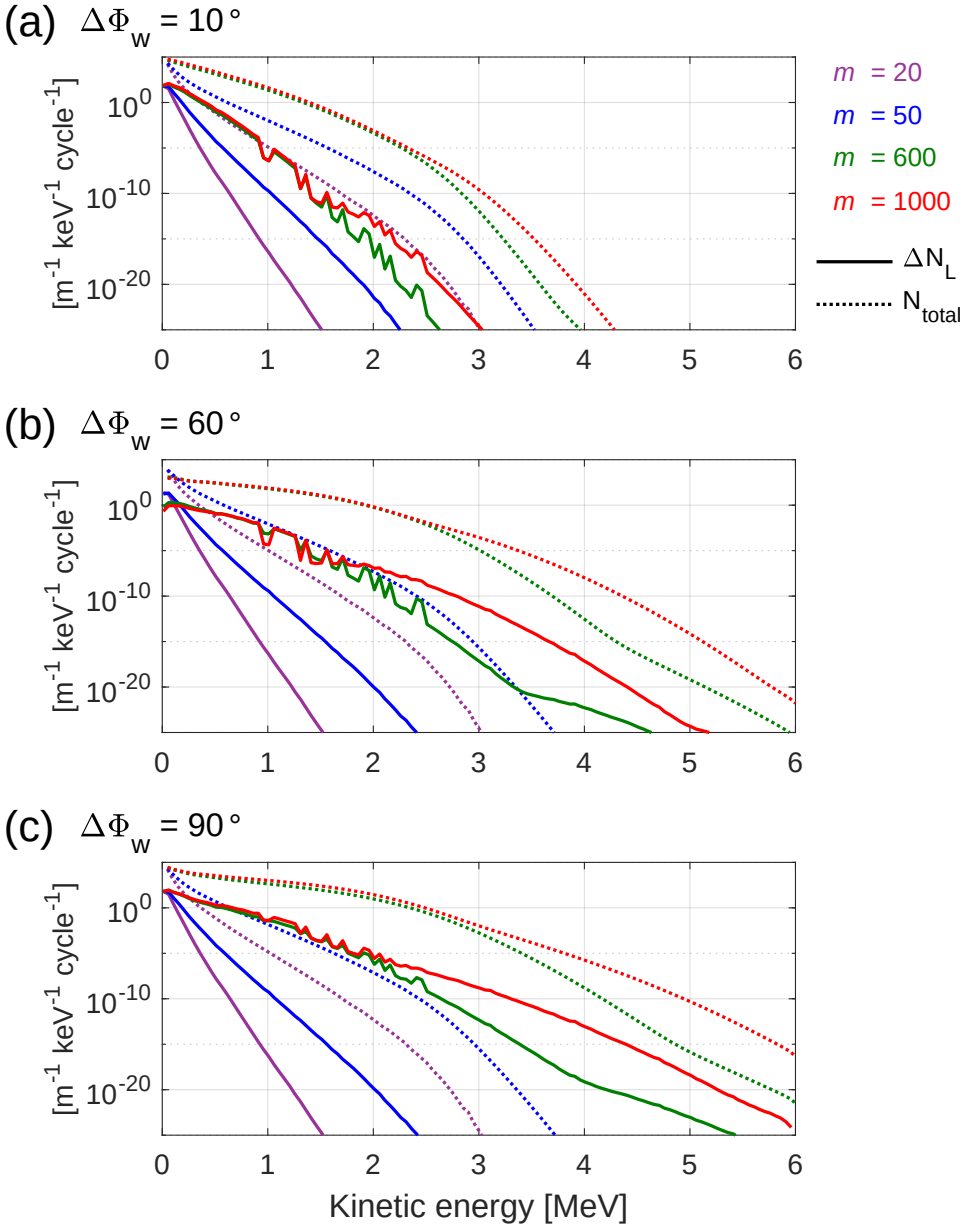

Figure 4. The precipitation rate ΔN_L and the total electron fluxes N_{total} corresponding to Figure 2 as functions of kinetic energy for (a) $\Delta\Phi_w = 10°$, (b) $\Delta\Phi_w = 60°$, and (c) $\Delta\Phi_w = 90°$. The solid lines represent ΔN_L and the dotted lines stand for N_{total}. The purple, blue, green, and red curves denote interaction cycles $m = 20, 50, 600$, and 1000, respectively.

3.1.2 Comparison among different wave normal angles

Applying the same initial distribution function, influx functions, and longitudinal chorus generation range for $\Delta\Phi_w = 60°$ introduced in Section 3.1.1, we compare the convolution integral results for different Green's function sets. We plot the equatorial distribution functions F^{Φ}_{mEQ} with m = 20, 50, 600, and 1000 in Figure 5 and also plot their corresponding cross-sections in Figure 6. In Figure 5a, we find that electrons are accelerated to MeV level rapidly in Case 3, and in Figure 5c we have electron more than 4 MeV in Case 1. The result are similar to what we have presented in Hsieh et al. (2020), in which the simulations are performed in a one-dimensional background magnetic field. Since that purely parallel chorus emissions can accelerate electrons to $>$ 4 MeV faster than the other cases, the re-acceleration effect of Case 1 is stronger than the other 2 cases (see Figures 6c and 6d).

The precipitation rate ΔN_L and the total fluxes N_{total} as functions of kinetic energy K are shown in Figure 7. The configuration of Figure 7 is the same as Figure 4. According to Figure 4 and Figure 7, we conclude that chorus emissions contribute to energetic electron precipitation for a wide energy range from tens of keV to a few MeV. However, the number of electrons precipitated into the loss cone is much smaller than that of electrons being accelerated and remaining in the radiation belt. By comparing Figures 7a–c, we find that oblique chorus waves make more electron precipitation than parallel chorus waves at $K < 3$ MeV. It is interesting that after hundreds of cycles of interaction, the purely parallel chorus emissions lead to noticeable precipitation at $K >$ 3 MeV, which does not appear in the oblique cases. However, the value of $K > 3$ MeV precipitation of Case 1 is small compared with the precipitations at $K < 1$ MeV.

We integrate the precipitation fluxes over K, α_L, Φ for each cycle m and plot the normalized precipitation rate N_L/N_T for 3 minutes in Figure 8. The N_L is given by

$$N_L = \sum_K \Delta N_L \Delta K \ , \tag{9}$$

and N_T, the total electron fluxes in the system, is written as

$$N_T = \sum_K \sum_\alpha \sum_\Phi f_m(K, \alpha, \Phi) \tilde{A}(K, \alpha_T) R_{EQ} \Delta\Phi \Delta\alpha \Delta K \ . \tag{10}$$

We convert the precipitation rate from per cycle to per second in Figure 8 according to the time scale of one-cycle of interaction(0.66 seconds). Figures 8a–d compare the energetic electron precipitation among the 3 cases at different energy ranges, which are (a) $K < 100$ keV, (b) 100 keV $\leq K <$ 500 keV, (c) 0.5 MeV $\leq K <$ 1 MeV, and (d) $K \geq 1$ MeV. The blue, green, and red curves stand for Case 1, Case 2, and Case 3, respectively. For all cases, most of the precipitation occurs in $K < 100$ keV. Precipitation rates for $K >$ 1 MeV is much less than that for $K < 100$ keV. This phenomenon agrees with the observation reviewed by Tsurutani et al. (2013).

Furthermore, in each energy range, the precipitation affected by oblique chorus emissions is greater than those affected by parallel chorus emissions, and the electron precipitation ratio (oblique case/parallel case) becomes larger for greater electron energies. At $K < 100$ keV, it is interesting that precipitation in Case 2 is greater than that in Case 3. The reason is that in Case 3, many low α electrons move to higher energy through the n=0 Landau resonance, the number of electrons remaining in $K < 100$ keV for Case 3 is less than that for other cases. Figures 8b–d indicate that if we want to find sub-relativistic or relativistic electron precipitation induced by chorus emissions, it requires several consecutive emissions to make the K of electrons great enough and the α of electrons low enough. It is very difficult to have relativistic electron precipitation by a single chorus emission or a few emissions.

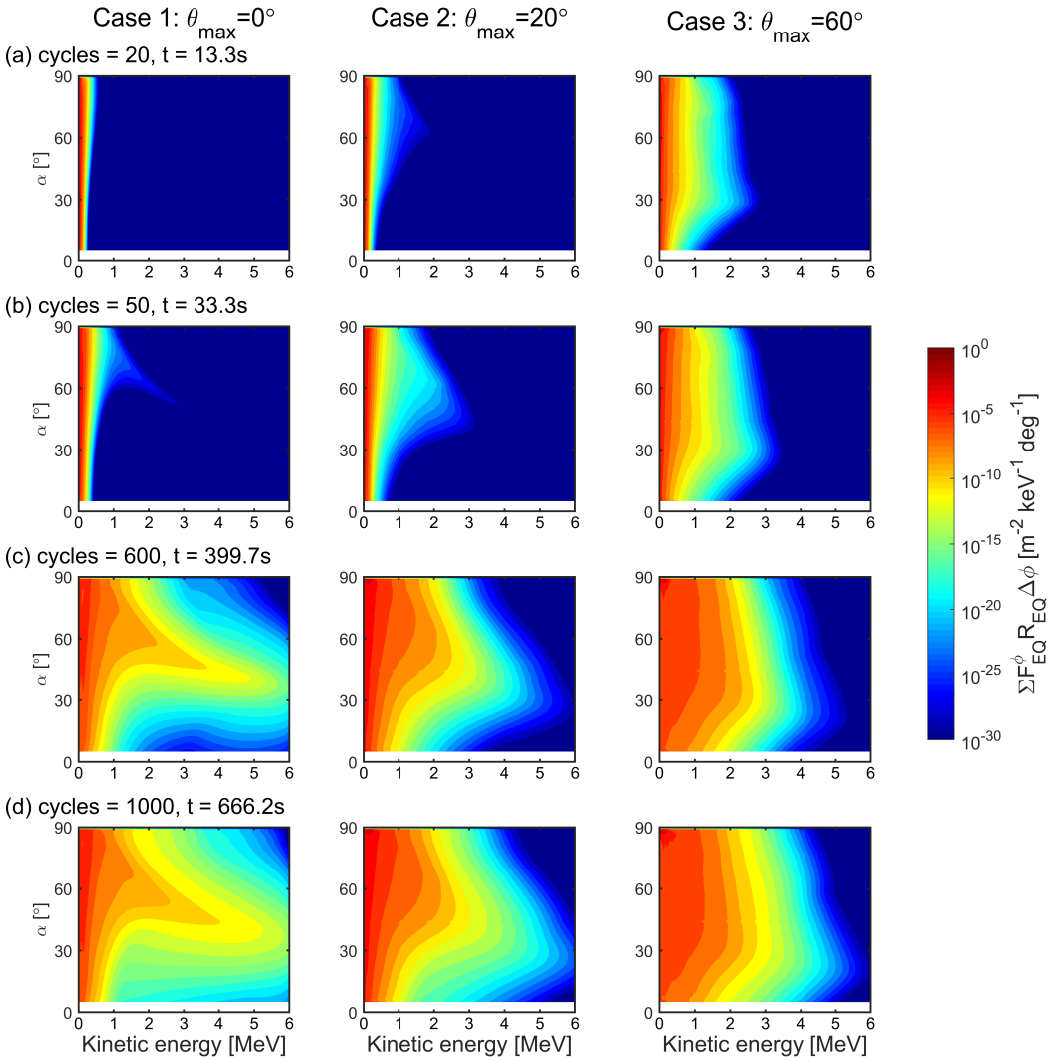

Figure 5. (a–d) Time evolution of the equatorial electron distribution functions $F^{\Phi}_{mEQ}(E, \alpha, \Phi)$ summed over the longitudinal direction for $\Delta\Phi_w$=60° after m cycles of interaction with parallel chorus emissions (left column) or with oblique chorus emissions (middle and right columns). The initial equatorial distribution function $F^{\Phi}_{0EQ}(E, \alpha, \Phi)$ is set as a static distribution whose energy ranges from 10 to 30 keV, equatorial pitch angle ranges from 5° to 89°, and longitudinal ranges from 0° to 60°. These integrations of F^{Φ}_{0EQ} over E, α, and the longitude are normalized to $1m^{-2}$.

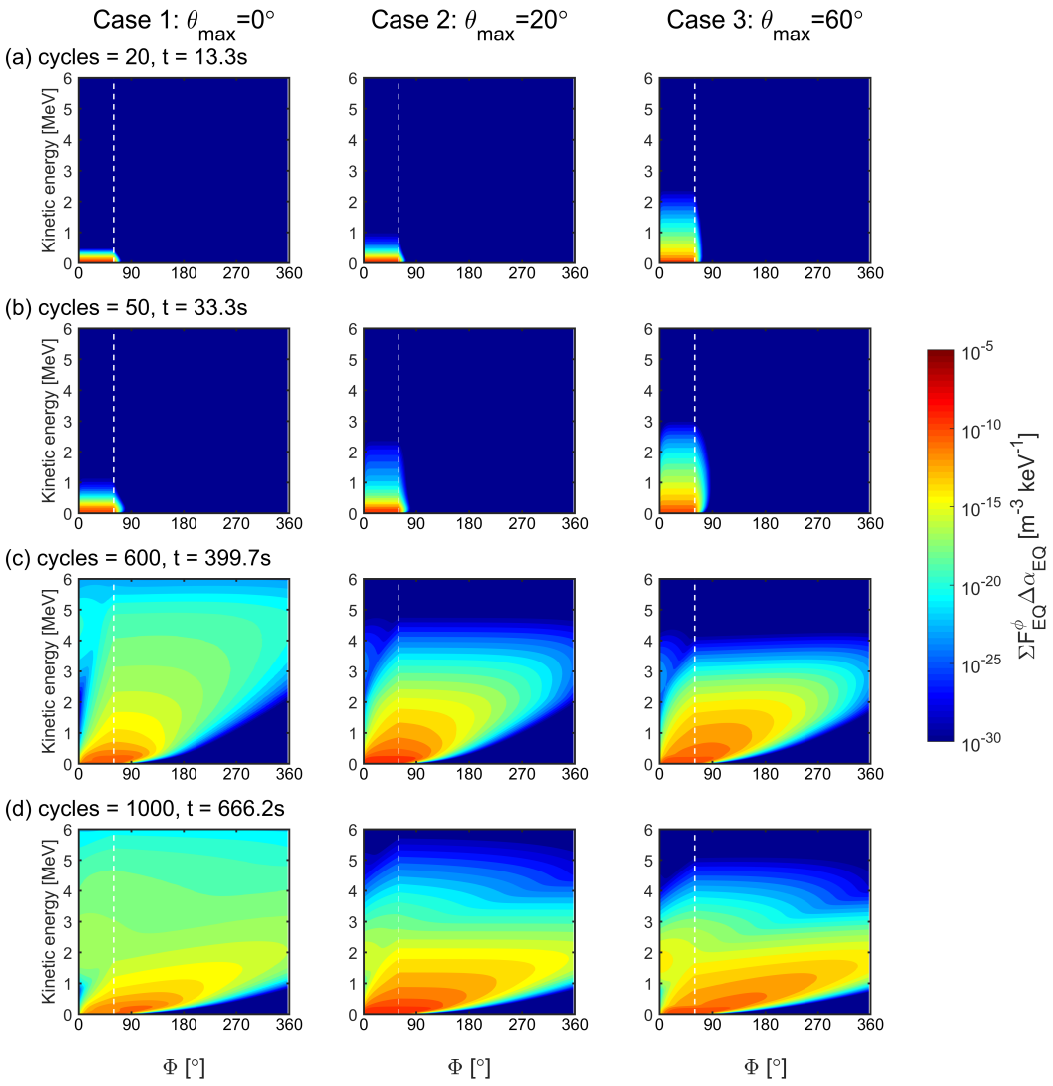

Figure 6. (a–d) Time evolution of the equatorial electron distribution functions $F^{\Phi}_{mEQ}(E, \alpha, \Phi)$ summed over the equatorial pitch angle α from 5° to 89° as functions of longitudinal angle Φ and kinetic energy K for Case 1 (left panels), Case 2 (middle panels), and Case 3 (right panels). The chorus emissions exist in longitudinal ranges $\Delta\Phi_w = 60°$ as shown by white dashed lines.

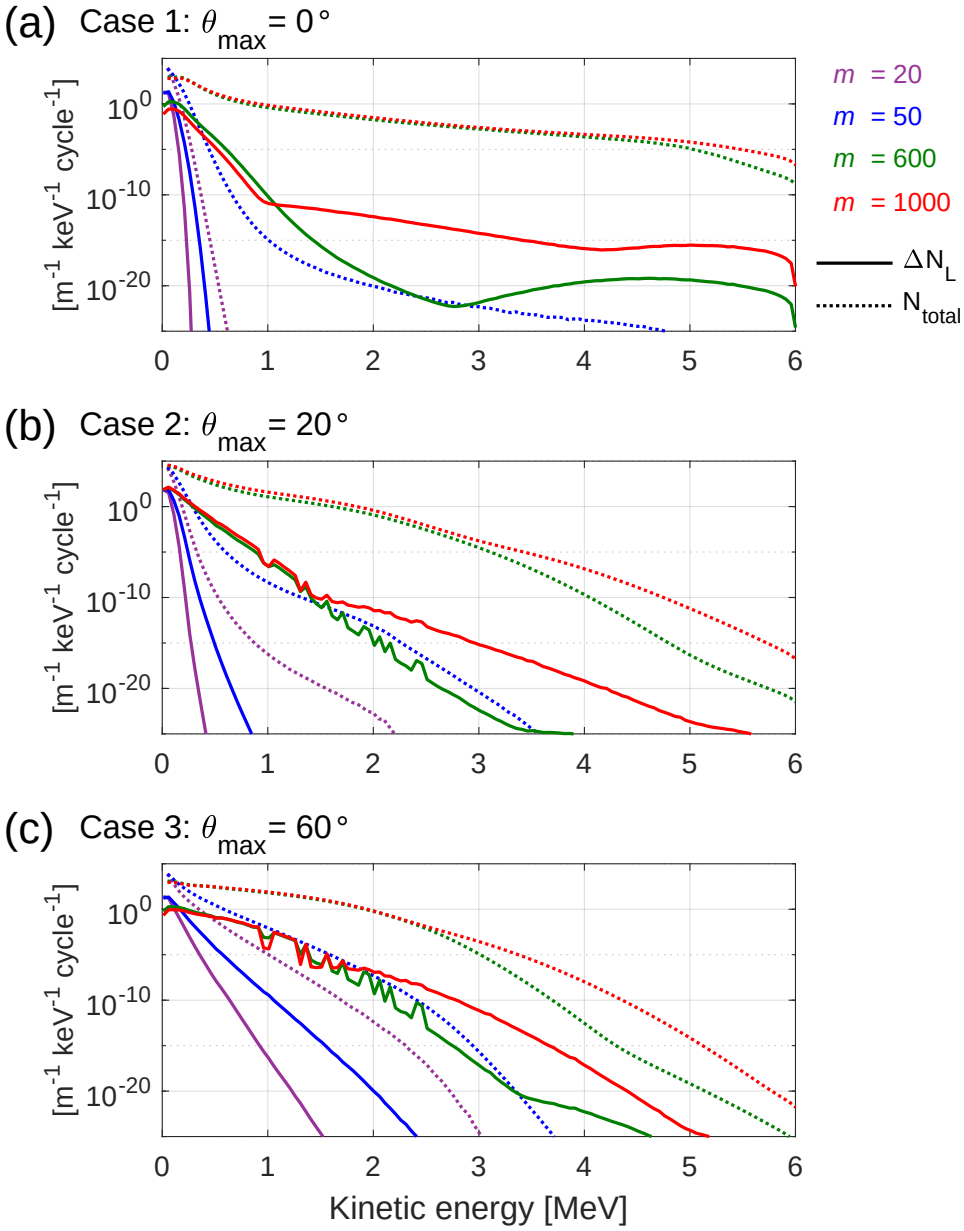

Figure 7. The precipitation rate ΔN_L and the total electron fluxes N_{total} corresponding to Figure 5 as functions of kinetic energy for wave models (a) Case 1: θ_{max}=0°, (b) Case 2: θ_{max}=20°, and (c) Case 3: θ_{max}=60°. The solid lines represent ΔN_L and the dotted lines stand for N_{total}. The purple, blue, green, and red curves denote interaction cycles $m = 20, 50, 600$, and 1000, respectively.

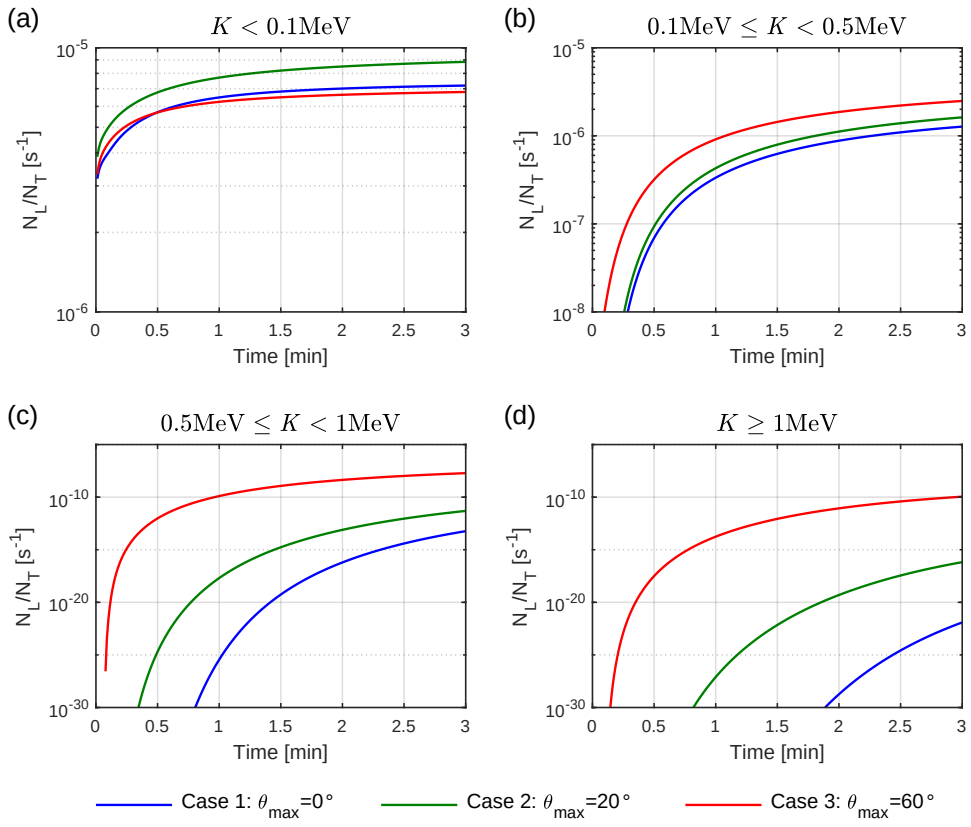

Figure 8. Electron precipitation rates (per second) normalized by trapped electrons N_T with respect to the distribution functions shown in Figure 5. The precipitation rates are calculated with the energy range (a) $K < 100$ keV, (b) 100 keV $\leq K <$ 500 keV, (c) 0.5 MeV $\leq K <$ 1 MeV and (d) $K \geq 1$ MeV. The red, green and blue lines represent Case 1–3, respectively.

3.2 Electrons initially at high equatorial pitch angle

When geomagnetic substorm occurs, there are energetic particles with high equatorial pitch angle injected into the inner magnetosphere from the magnetic tail (e.g., Baker et al., 1982; Reeves et al., 1990; X. Li et al., 1998; Turner et al., 2017, and references therein). We study how fast these high equatorial pitch electrons get into the loss cone via chorus wave-particle interactions. Figure 9 shows the time evolution of electron fluxes initially at K=10–30 keV and α=70–89°, which represent tens of keV and high equatorial pitch angle electrons, interacting with the 3 cases. Here the $\Delta\Phi_w$ is 60°, and the initial fluxes integrated over E, α, and Φ are also normalized to $1m^{-2}$. Figures 9a–c stand for interaction cycles equal to 1–3, respectively. The high equatorial pitch angle electrons fall into the loss cone (the white area at the bottom of the figures) after interacting with 3 chorus emissions, whose time scale is about 2 seconds, for all 3 cases. It is clear that the number of precipitation electrons for oblique chorus emissions is more than that for parallel emissions, and the precipitate electrons of the oblique cases contain higher energy than those of the parallel case. Especially for Case 3, there is an obvious Landau branch causing higher energy electrons and eventually the combination of the Landau resonance and cyclotron resonance makes the higher energy pattern at a wide range of equatorial pitch angle. Figure 10 is similar to Figure 9 but the initial energy is 0.99–1.01 MeV, which represent relativistic electrons. Figures 10a–c show interaction cycles of 1, 5, and 10, respectively. Comparing with tens of keV electrons, nonlinear scattering and nonlinear trapping for relativistic electrons cannot lower the equatorial pitch angle effectively. Even after 10 cycles (about 7 seconds), no electron is dropped to the loss cone in all three cases. Therefore, the EEP at MeV level is much difficult than that at tens of keV level. However, Figure 10c indicates that oblique chorus emissions make relativistic electrons move to lower α more efficiently than parallel chorus emissions, resulting in higher probability of precipitation.

Figure 9 and Figure 10 imply three things: (1) Electron precipitation at tens of keV is much easier than that at MeV. (2) Oblique chorus emissions contribute to more electron precipitation. (3) If the initial electron conditions are the same, precipitated electrons induced by oblique chorus reach higher energy than that induced by the purely parallel chorus.

4 Discussion

We check the resonance condition at different latitudes to verify the relations among K, α, and Lat during the electron precipitation process. The perpendicular velocity of a resonant electron is given by

$$v_\perp = V_R \tan\alpha_h \ , \tag{11}$$

where α_h is the local pitch angle. Then, the Lorentz factor of a resonant electron is written as

$$\gamma = \frac{K}{m_0c^2} + 1 = \frac{1}{\sqrt{1-\frac{V_R^2+v_\perp^2}{c^2}}} = \frac{c}{\sqrt{c^2 - V_R^2\sec^2\alpha_h}} \ . \tag{12}$$

The relation between local equatorial pitch angle α_h and equatorial pitch angle α is

$$\sin\alpha = \sqrt{\frac{B_{0eq}}{B_0(h)}}\sin\alpha_h \ . \tag{13}$$

According to (11), (12), and (13), we derive equatorial pitch angles α as functions of electron kinetic energy K for the nth resonance as

$$\alpha = \sin^{-1}\left[\sqrt{\frac{B_{0eq}}{B_0(h)}}\sqrt{1-\left(\frac{\omega}{ck_\parallel}\right)^2\frac{(\gamma - n\Omega_e/\omega)^2}{\gamma^2-1}}\right] \ . \tag{14}$$

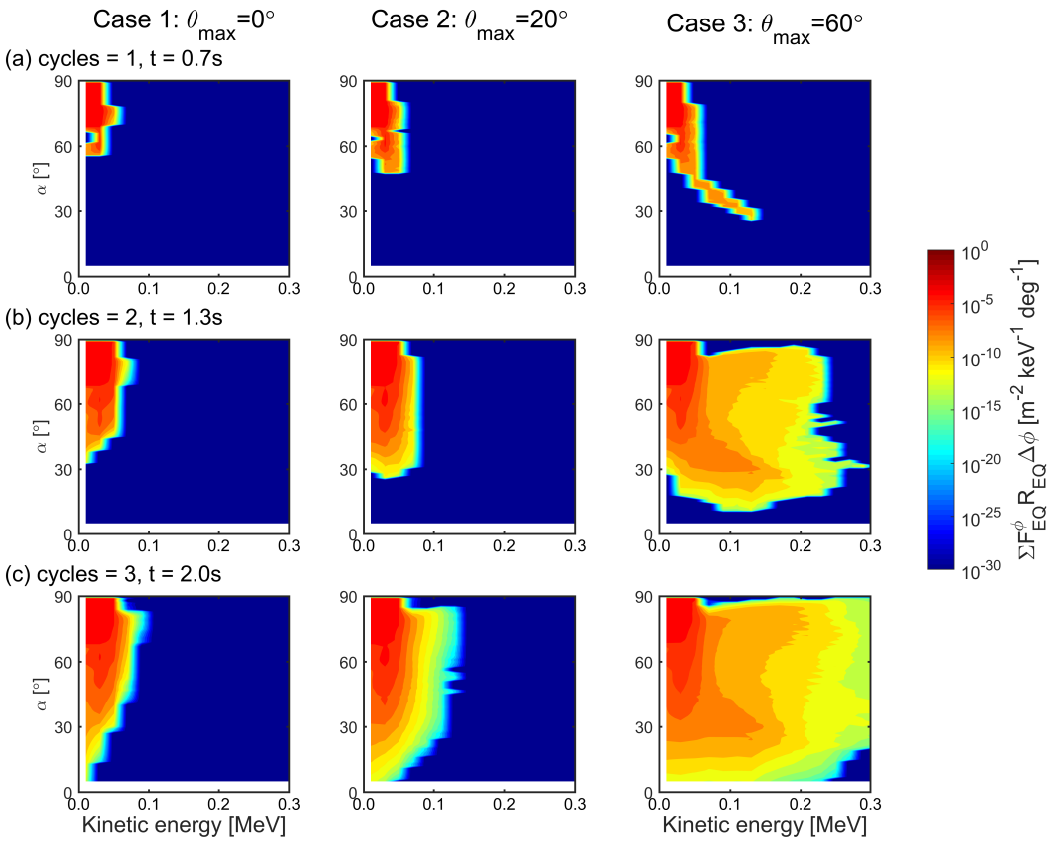

Figure 9. The equatorial electron distribution functions $F^{\Phi}_{mEQ}(E, \alpha, \Phi)$ summed over the longitudinal direction for $\Delta\Phi_w$=60° after 1–3 cycle of interactions for Cases 1–3. The initial distribution function $F^{\Phi}_{0EQ}(E, \alpha, \Phi)$ is a static distribution whose energy ranges from 10 to 30 keV, equatorial pitch angle ranges from 70° to 89°, and longitudinal ranges from 0° to 60°.

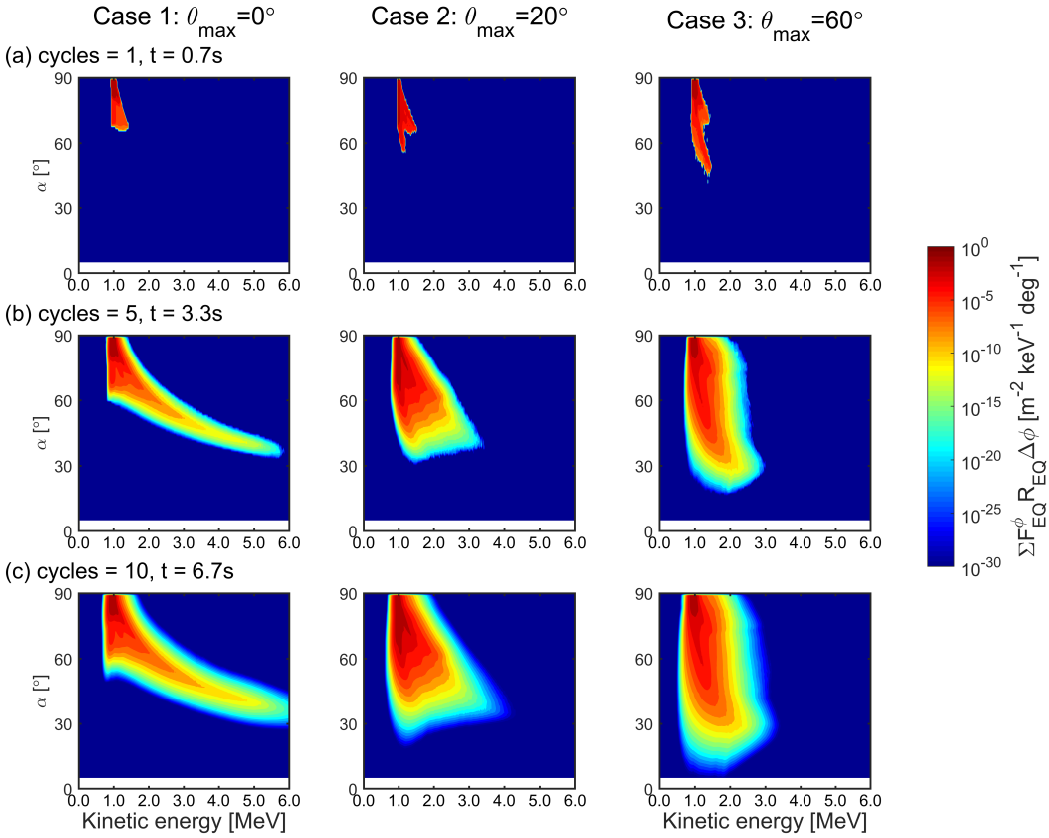

Figure 10. The equatorial electron distribution functions $F^{\Phi}_{mEQ}(E, \alpha, \Phi)$ summed over the longitudinal direction for $\Delta\Phi_w$=60° after 1, 5, and 10 cycle of interactions for Cases 1–3. The initial distribution function $F^{\Phi}_{0EQ}(E, \alpha, \Phi)$ is a static distribution whose energy ranges from 0.99 to 1.01 MeV, equatorial pitch angle ranges from 70° to 89°, and longitudinal ranges from 0° to 60°.

The parallel wave number $k_{\parallel}$ is derived by the Appleton-Hartree equation, which is the dispersion relation of whistler mode equation. We plot the solutions of equation (14) at different latitudes for resonances with harmonic numbers n=0, 1, −1, and 2 in Figures 11a–d, respectively. The parallel wave number $k_{\parallel}$ follows the value of Case 3. The blue, green, red, and magenta lines respectively stand for $Lat = 0°$, 15°, 30°, and 40°. The arrows in Figures 11a and 11b point out the scattering tendency for electrons undergoing the nonlinear trapping according to the Green's function set of Case 3 as references. It is worth noting that at high latitudes the nonlinear trapping becomes very difficult because of the large gradient of the background magnetic field. In Figure 11a, in low α part all the curves appear at very low energy, indicating that the electron loss through the n=0 Landau resonance only occurs at low energy, namely, below 100 keV. In other words, for > 100 keV electrons, they have difficulty being pushed into the loss cone by the $n = 0$ Landau resonance. The curves also imply that the interaction via the $n = 0$ resonance occurs in a wide range of latitude. Figure 11b points out that electron precipitation induced by the $n = 1$ cyclotron resonance can take place from a few keV to about 3 MeV. In addition, precipitated electrons with higher energies must correspond to interaction positions with higher latitudes. This description is the same as the conclusion reported by Miyoshi et al. (2015).

In Figures 11c and 11d we can find that $n = -1$ and $n = 2$ resonance might contribute to EEP for a wide energy range as well. In Hsieh and Omura (2017b) we do found EEP caused by nonlinear trapping of the $n = -1$ (see Figures 8f and 9f of Hsieh and Omura (2017b)), but it requires very large amplitude and long wave packet. Compared with the $n = 0$ and 1 resonances, direct contributions to EEP by $n = -1$ and 2 resonances are very small.

The solutions of equation (14) at different latitudes for the $n = 1$ cyclotron resonance with different ratios of electron plasma frequency to cyclotron frequency ratio ω_{pe}/Ω_{e0} are plotted in Figure 12. The $k_{\parallel}$ follows the value of Case 1. The arrows in Figure 11b point out the scattering tendency for electrons undergoing the nonlinear trapping based on the Green's function set of Case 1. Focusing on the low α part, if the ω_{pe}/Ω_{e0} ratio is greater, the cyclotron resonance becomes more concentrated to the lower energy part, indicating that the precipitation rate of relativistic electrons is high for low ω_{pe}/Ω_{e0} ratio and low for high ω_{pe}/Ω_{e0}. In Figure 11d, high ω_{pe}/Ω_{e0} ratio denotes plasmaspheric hiss, which locates in higher plasma density regions. The EEP induced by hiss at energy < 1 MeV is a remaining issue for future studies.

Then, we calculate the resonant energy for the electron near the loss cone $\alpha = 4.56°$. Combining equations (1), (11), and (12), we have

$$\left(\tilde{U}^2 - 1\right)\gamma^2 + 2n\frac{\Omega_e}{\omega}\gamma - \left(\tilde{U}^2 + n^2\frac{\Omega_e^2}{\omega^2}\right) = 0 \ , \tag{15}$$

where $\tilde{U} = \frac{c}{V_{p\parallel}}\cos\alpha_h$, and $V_{p\parallel} = \omega/k_{\parallel}$ is the parallel phase velocity. Solving equation (15), we obtain

$$K = m_0c^2\left(\frac{-n\frac{\Omega_e}{\omega} + \sqrt{(n\frac{\Omega_e}{\omega})^2 + (\tilde{U}^2 - 1)(\tilde{U}^2 + n^2\frac{\Omega_e^2}{\omega^2})}}{\tilde{U}^2 - 1} - 1\right) \ . \tag{16}$$

We plot the result for equation (16) for both $n = 0$ and $n = 1$ in Figure 13 according to the parameters of Case 3. The solid and dotted lines are for wave frequencies $\omega = 0.25$ and 0.5 Ω_{e0}, respectively. The blue curves stand for the $n = 0$ Landau resonance with $\alpha = \alpha_{loss}$ and the red curves denote the n =1 cyclotron resonance with $\alpha = \alpha_{loss}$. Since the wave phase velocity $V_{p\parallel}$ does not change much with different θ, Figure 13 is a good reference for chorus emissions with various θ. We find that resonant energy of the $n =$ 1 cyclotron resonance is always greater than that of the $n = 0$ Landau resonance at all

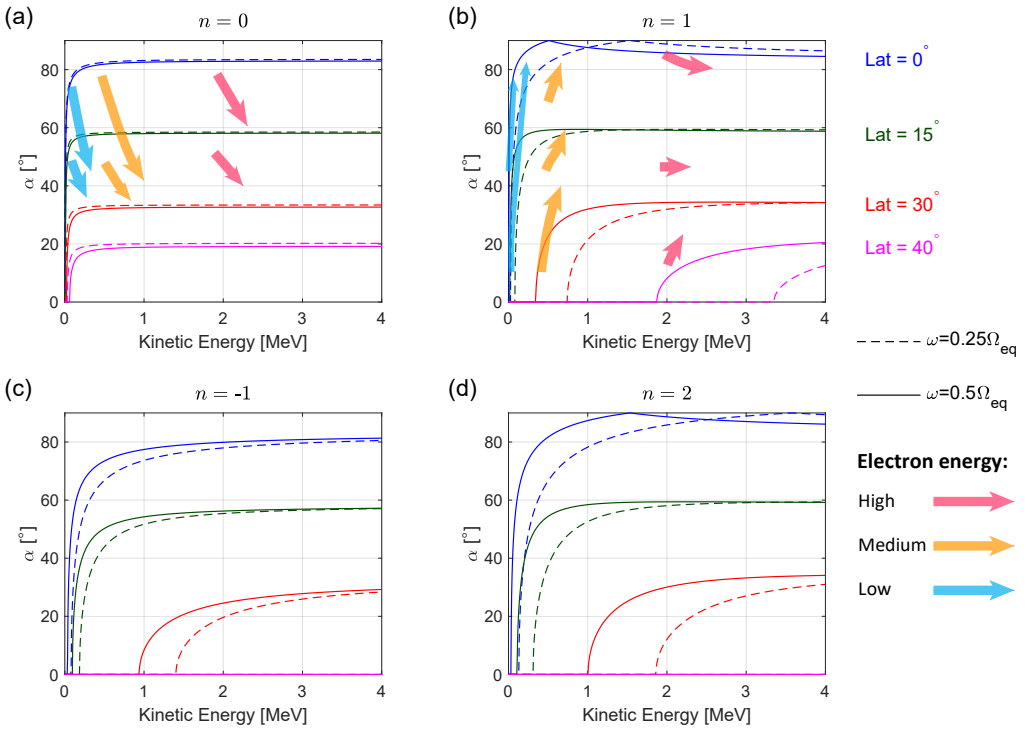

Figure 11. Solutions of equation (14) as resonance curves for $n = -1$ to 2 resonances at $Lat = 0^\circ$ (blue), $Lat = 15^\circ$ (dark green), $Lat = 30^\circ$ (red), and $Lat = 40^\circ$ (magenta). The dashed and solid curves indicate solutions for $\omega = 0.25$ and 0.5 Ω_{e0}, respectively. The electron plasma frequency to cyclotron resonance ratio is 4. Scattering tendencies of nonlinear trapped electrons are denoted by arrows for $n = 0$ and 1. Right blue arrows stand for tens of keV electrons, orange arrows denote hundreds of keV electrons, and pink arrows represent MeV electrons.

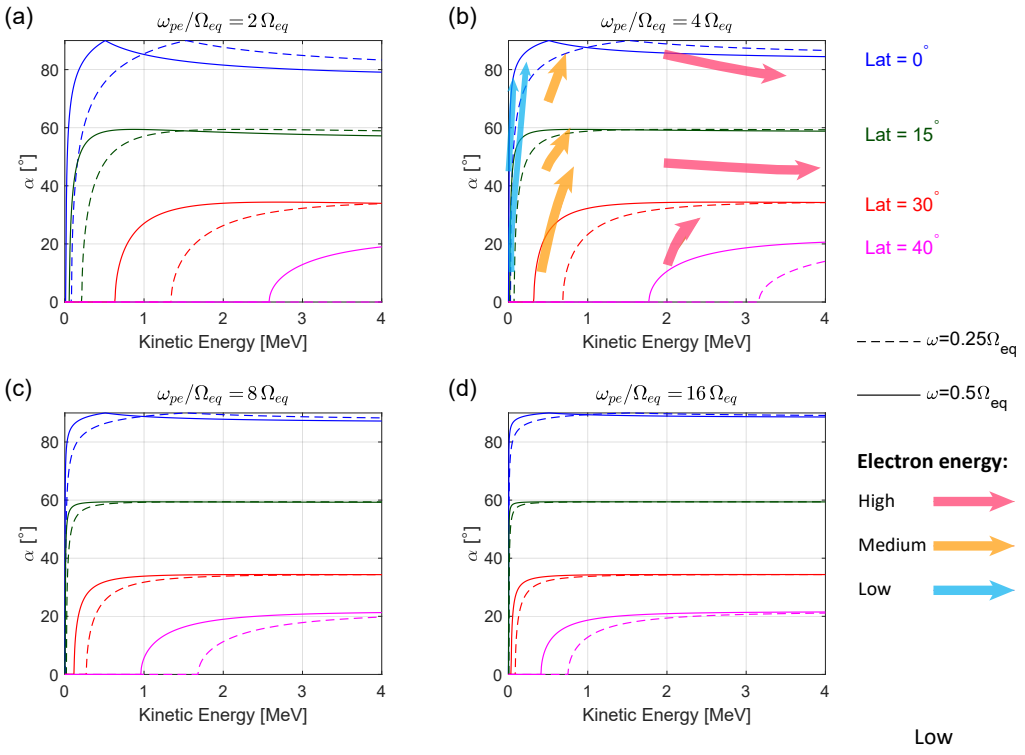

Figure 12. Solutions of equation (14) as resonance curves for $\omega_{pe}/\Omega_{e0} = 2$, 4, 8, and 16, for $n = 1$ resonances at $Lat = 0^\circ$ (blue), $Lat = 15^\circ$ (dark green), $Lat = 30^\circ$ (red), and $Lat = 40^\circ$ (magenta). The dashed and solid curves indicate solutions for $\omega = 0.25$ and 0.5 Ω_{e0}, respectively. Scattering tendencies of nonlinear trapped electrons for $\omega_{pe}/\Omega_{e0} = 4$ case are denoted by arrows in Figure 12b. Blue arrows stand for tens of keV electrons, orange arrows denote hundreds of keV electrons, and pink arrows represent MeV electrons.

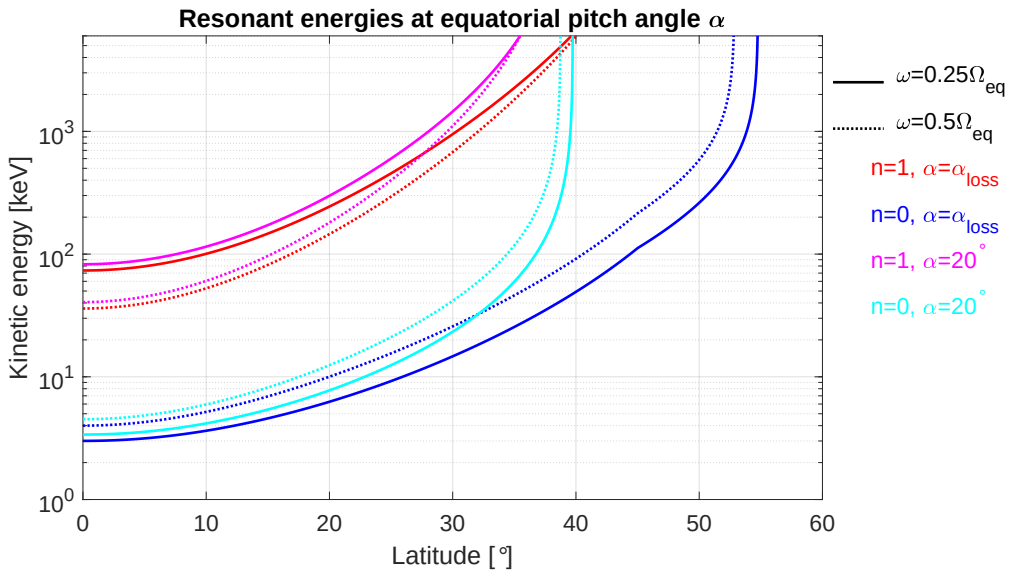

Figure 13. Resonant energies for electrons at equatorial pitch angle α as functions of Latitude for Case 3. The red and blue curves stand for the results at $\alpha = \alpha_{loss}$ for the $n = 1$ cyclotron resonance and the $n = 0$ Landau resonance, respectively. The solid lines are for wave frequency $\omega = 0.25\Omega_{e0}$, and the dotted lines denote $\omega = 0.25\Omega_{e0}$. The magenta and cyan cures denote resonant energies at $\alpha = 20°$ for the $n = 1$ cyclotron resonance and the $n = 0$ Landau resonance, respectively.

latitudes. We plot magenta curves representing the resonant energy for the $n = 1$ cyclotron resonance at $\alpha = 20°$ because the $n = 1$ cyclotron resonance can drop electrons to the loss cone from $\alpha = 20°$ based on the trajectories on Figure 1d. The magenta curves show higher resonant energies than the red curves. As a reference, we also plot cyan curves representing the $n = 0$ Landau resonance for electrons at $\alpha = 20°$. At energy > 100 keV, the blue curves relate to $Lat > 40°$, where it is difficult to have strong resonance. Because of the large gradient of the background magnetic field, which makes the inhomogeneity factor very large (Omura et al., 2019), we only have very weak resonance at high latitudes. Because the nonlinear trapping of the $n = 1$ cyclotron resonance cannot lower the equatorial pitch angle of electrons, the precipitation is all done by nonlinear scattering. Therefore, we conclude that most of the EEP cases are directly pushed by nonlinear scattering of the $n = 1$ cyclotron resonance. The $n = 0$ Landau resonance only contributes to a small portion of precipitation at $K < 100$ keV. We examine trajectories of the precipitation electrons for several Green's functions. We find that the number of EEP cases directly done by the $n = 0$ Landau resonance is much smaller than that directly done by the $n = 1$ cyclotron resonance.

However, our convolution integral results show that EEP cases induced by oblique chorus emissions is more than that induced by parallel chorus emissions. In oblique whistler mode wave-particle interactions, an electron can go through not only $n = 1$ cyclotron resonance but also the $n = 0$ Landau resonance and higher-order resonances of multiple emissions during a bounce motion. Hence, the electron interacting with a oblique chorus has more opportunity to move toward a lower equatorial pitch angle than that interacting with a purely parallel chorus. The $n = 0$ Landau resonance can move electrons from high α to low α via the nonlinear trapping effectively as demonstrated in Figure 10. On the other hand, the $n = 1$ or $n = 2$ cyclotron can lower electron's α via

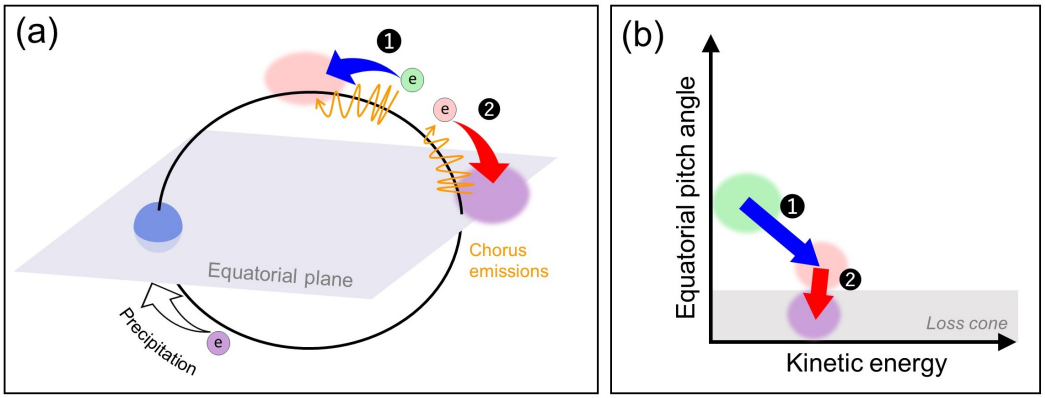

Figure 14. Schematic pictures of the wave-particle interactions between chorus emissions and an electron showing the precipitation process by multiple resonances of different emissions. (a) Schematic picture along a field line. (b) Schematic picture showing the kinetic energy and equatorial pitch angle tendency during the process. The 2 steps of precipitation process are: (1) A high equatorial pitch angle electron gets energy and its equatorial pitch angle becomes lower via nonlinear trapping of Landau resonance. (2) The electron is pushed into the loss cone via nonlinear scattering of cyclotron resonance. The green, pink, and purple patterns stand for the electron status before step 1, after step 1, and after step 2, respectively. After step 2, the electron precipitates at the opposite hemisphere.

nonlinear scattering process. Finally, after a few cycles of interaction, an electron moves close to α_{loss} and then be pushed into the loss cone by the $n = 1$ cyclotron resonance. A schematic picture explaining this process is plotted in Figure 14. Figure 14a shows a sketch along a field line, and Figure 14b illustrates the process in the K–α phase space. The two steps of the energetic electron precipitation for oblique whistler mode wave-particle interactions are: (1) A high equatorial pitch angle electron obtains energy from a chorus emission and its equatorial pitch angle becomes lower via nonlinear trapping of Landau resonance. (2) The electron bounces back toward the equator and then is pushed into the loss cone via the nonlinear scattering of cyclotron resonance by another emission. The green, pink, and purple patterns in Figure 14 stand for the electron status before step 1, after step 1, and after step 2, respectively. After the electron moved to the loss cone, it precipitates in the opposite hemisphere if there is no other process making its equatorial pitch angle larger.

Although subpacket structure of chorus emissions allows electrons undergo multiple resonances within one wave packet (Hsieh et al., 2020), the 2-step precipitation process cannot finish within one wave packet. Figure 13, which is derived from the first order resonance condition, shows that the interaction latitude of the $n = 0$ Landau resonance is higher than that of the $n = 1$ cyclotron resonance for electrons at the same energy. Nonlinear trapping via the Landau resonance occurs when an electron and a chorus emission move in the same direction along a field line. The Landau resonance brings the resonant electron to higher latitude. Hence, the step 2 must happen at least after the electron bounces back from the mirror point.

In considering the second order resonance condition, the inhomogeneity factor S_n is an important factor controlling the nonlinear interactions in both $n = 0$ and $n = 1$

resonances given by

$$S_n = -\frac{1}{\Omega_{t,n}^2}\left\{\left(1-\frac{V_R}{V_{g\parallel}}\right)^2\frac{\partial\omega}{\partial t}+\left[\frac{\omega v_\perp^2}{2\Omega_e V_{p\parallel}}-\frac{n}{\gamma}V_R\left(1+\frac{\Lambda\chi^2[\Omega_e-(\gamma/n)\omega]}{2(\Omega_e-\omega)}\right)\right]\frac{\partial\Omega_e}{\partial z}\right\}. \tag{17}$$

Detailed explanation of parameters in S_n is given by equation (165) of Omura (2021). In the 2-step precipitation process, we need $|S_0| < 1$ for the nonlinear trapping (step 1) and $|S_1|$ around 1 for the effective nonlinear scattering (step 2). The second term of equation (17) shows the effect of the gradient of the background magnetic field and this term is smaller when $n = 0$ then that when $n \neq 0$, resulting in that the latitudinal range for $|S_0| < 1$ is wider than that for $|S_1|$ around 1.

Besides, an electron with lower equatorial pitch angle has longer bounce period, which means that it takes more time for the bounce-backed electron to reach the interaction latitude for the $n = 1$ cyclotron resonance. Taking the timescale of a single chorus emission, group velocity, and electron bounce period into account, when an electron after step 1 bounces back to the low latitude, where the cyclotron resonance should occur, the tail of the same chorus emission has already left. Therefore, after step 1, an resonant electron has no chance to interact with the same chorus emission via the $n = 1$ cyclotron resonance. In other words, this precipitation process cannot be completed within a single emission.

5 Summary

We performed test particle simulations of energetic electrons interacting with oblique whistler mode chorus emissions in a three-dimensional dipole field. By calculating the Green's functions and taking convolution integrals for 3 chorus wave models with different wave normal angle variations, we compared the precipitation rates among cases with purely parallel propagation and oblique propagation.

Our findings regarding energetic electron precipitation (EEP) are listed as follows:

1. Most of the EEP events are less than 100 keV. We also find EEP for relativistic electrons but the fluxes are much smaller than those of electrons less than 100 keV (See Figure 8).
2. Most of the EEP events are directly caused by the nonlinear scattering of the $n = 1$ cyclotron resonance.
3. Nonlinear trapping of the n=0 Landau resonance also directly contributes to EEP at $K < 100$ keV, but the number of the cases is much less than that of the EEP directly caused by nonlinear scattering of the n=1 cyclotron resonance.
4. For electrons $<$ 0.1 MeV, the precipitation is very prompt within a time scale of a few emissions (a few seconds). For electrons $>$ 0.1 MeV, the precipitation requires interactions with tens or hundreds chorus emissions (a few minutes).
5. Obliquely propagating chorus emissions cause more EEP than parallel propagating chorus emissions through the following 2-step EEP process:
   (1) During the first chorus emission, a high equatorial pitch angle electron obtains energy and its equatorial pitch angle becomes lower via nonlinear trapping due to Landau resonance.
   (2) The electron bounces back toward the equator and then is pushed into the loss cone via the nonlinear scattering due to cyclotron resonance with another chorus emission.

Although we find that chorus emissions can cause the precipitation of electrons in the outer radiation belt, the fluxes are extremely small for MeV electrons (see Figure 4). We will calculate evolution of electron fluxes interacting with both whistler mode chorus and electromagnetic ion cyclotron (EMIC) waves, which makes remarkable contri-

489 butions to relativistic electron loss (e.g., S. Nakamura et al., 2019), in the future to un-
490 derstand more about the formation and loss processes of the outer radiation belt.

491 Appendix A Wave magnetic field and electric field components in a
492 dipole magnetic magnetic field

493 The wave magnetic field and electric field in a field-align frame are given by

$$\begin{aligned} 494 \quad \mathbf{B_w} &= \mathbf{e_{x''}} B''_x + \mathbf{e_{y''}} B''_y + \mathbf{e_{z''}} B''_z \\ 495 &= \mathbf{e_{x''}} B^w_x \cos\psi + \mathbf{e_{y''}} B^w_y \sin\psi - \mathbf{e_{z''}} B^w_z \cos\psi\,, \end{aligned} \tag{A1}$$

496

$$\begin{aligned} 497 \quad \mathbf{E_w} &= \mathbf{e_{x''}} E''_x + \mathbf{e_{y''}} E''_y + \mathbf{e_{z''}} E''_z \\ 498 &= \mathbf{e_{x''}} E^w_x \sin\psi - \mathbf{e_{y''}} E^w_y \cos\psi + \mathbf{e_{z''}} E^w_z \sin\psi\,, \end{aligned} \tag{A2}$$

499 where $\mathbf{e_{x''}}$, $\mathbf{e_{y''}}$, and $\mathbf{e_{z''}}$ are unit vectors in the x, y, and z directions of the field-align
500 coordinate. The $\mathbf{e_{z''}}$ points out the direction of the background magnetic field line, the
501 $\mathbf{e_{x''}}$ is the outward (radial) direction of the field line, and the $\mathbf{e_{y''}}$ is eastward direction.
502 The local wave phase ψ is given by

$$503 \quad \psi_i(t) = \psi_0 + \int \omega(t)dt - \int_{h_0}^{h_i} k_\parallel dh - k_\perp r_L \cos(\phi')\,, \tag{A3}$$

504 where h is the distance along the field from the equator, r_L is gyroradius. The ϕ' is 90°
505 minus the gyrophase, and the way of obtaining the $\cos(\phi')$ is described later in Appendix
506 B. Note that the wave vector is at the $x'' - z''$ plane. The given wave magnetic field
507 amplitude B_w is written in the form

$$508 \quad B_w = \sqrt{(B^w_x \cos\psi)^2 + (B^w_y \sin\psi)^2 + (B^w_z \cos\psi)^2}\,. \tag{A4}$$

509 Tilt angle η is the angle between z-axis of the dipole field (North pole) and the background
510 magnetic field given by

$$511 \quad \eta = \mathrm{atan2}\left(\sqrt{B^2_{0x} + B^2_{0y}}, B_{0z}\right)\,. \tag{A5}$$

512 Converting the wave fields to the meridian plane, the wave magnetic fields are written
513 as

$$514 \quad \begin{bmatrix} B_{x'} \\ B_{y'} \\ B_{z'} \end{bmatrix} = \begin{bmatrix} \cos\eta & 0 & -\sin\eta \\ 0 & 1 & 0 \\ \sin\eta & 0 & \cos\eta \end{bmatrix} \begin{bmatrix} B_{x''} \\ B_{y''} \\ B_{z''} \end{bmatrix} \quad \text{for } z > 0 \text{ (Northern Hemisphere)}, \tag{A6}$$

515 and

$$516 \quad \begin{bmatrix} B_{x'} \\ B_{y'} \\ B_{z'} \end{bmatrix} = \begin{bmatrix} \cos\eta & 0 & \sin\eta \\ 0 & 1 & 0 \\ -\sin\eta & 0 & \cos\eta \end{bmatrix} \begin{bmatrix} B_{x''} \\ B_{y''} \\ B_{z''} \end{bmatrix} \quad \text{for } z < 0 \text{ (Southern Hemisphere)}. \tag{A7}$$

517 Setting the longitude $\Phi = 0°$ as $+x$ direction and $\Phi = 90°$ as $+y$ direction, we rotate
518 the wave magnetic field and obtain the wave field in the dipole field as

$$519 \quad \begin{bmatrix} B_x \\ B_y \\ B_z \end{bmatrix} = \begin{bmatrix} \cos\Phi & -\sin\Phi & 0 \\ \sin\Phi & \cos\Phi & 0 \\ 0 & 0 & 1 \end{bmatrix} \begin{bmatrix} B'_x \\ B'_y \\ B'_z \end{bmatrix}\,. \tag{A8}$$

520 Hence, the wave magnetic fields in the dipole field are written as

$$521 \quad \begin{bmatrix} B_x \\ B_y \\ B_z \end{bmatrix} = \begin{bmatrix} \cos\Phi & -\sin\Phi & 0 \\ \sin\Phi & \cos\Phi & 0 \\ 0 & 0 & 1 \end{bmatrix} \begin{bmatrix} \cos\eta & 0 & \mp\sin\eta \\ 0 & 1 & 0 \\ \pm\sin\eta & 0 & \cos\eta \end{bmatrix} \begin{bmatrix} B''_x \\ B''_y \\ B''_z \end{bmatrix}\,. \tag{A9}$$

For Northern/Southern Hemisphere, we apply the upper/lower part of the $\pm$ and $\mp$ signs in equation (A9). Coordinate transformation of wave electric fields (E_x, E_y, and E_Z) is the same as that of wave magnetic fields (B_x, B_y, and B_z).

The wave components in equations (A1) and (A2) are given by following relations.

$$\begin{aligned} B_x^w &= \frac{B_w}{\sqrt{\cos^2\psi + A_S^2\left(1 - A_P\tan\theta\right)^2\sin^2\psi + \tan^2\theta\cos^2\psi}} \\ B_y^w &= A_S(1 - A_P\tan\theta)B_x^w \\ B_z^w &= \tan\theta B_x^w \\ E_x^w &= A_S V_{p\parallel} B_x^w \\ E_y^w &= V_{p\parallel} B_x^w \\ E_z^w &= A_S A_P V_{p\parallel} B_x^w \ . \end{aligned} \tag{A10}$$

The dispersion relation of oblique whistler mode waves is given by

$$n_r^2 = \frac{c^2k^2}{\omega^2} = 1 - \frac{2X(1-X)}{2(1-X) - Y^2\sin^2\theta + Y\sqrt{Y^2\sin^4\theta + 4(1-X)^2\cos^2\theta}} \ , \tag{A11}$$

where

$$\begin{aligned} X &= \frac{\omega_{pe}^2}{\omega^2} \ , \\ Y &= \frac{\Omega_e}{\omega} \ . \end{aligned} \tag{A12}$$

The related variables in (A10) are derived from the dispersion relation (A11) as follows.

$$\begin{aligned} \tilde{S} &= 1 - \frac{\omega_{pe}^2}{\omega^2 - \Omega_e^2} \ , \\ \tilde{D} &= \frac{\omega_{pe}^2}{\omega^2}\frac{\omega\Omega_e}{\omega^2 - \Omega_e^2} \ , \\ \tilde{P} &= 1 - \frac{\omega_{pe}^2}{\omega^2} \ , \\ A_S &= \frac{n_r^2 - \tilde{S}}{\tilde{D}} \ , \\ A_P &= \frac{n_r^2\sin\theta\cos\theta}{n_r^2\sin^2\theta - \tilde{P}} \ . \end{aligned} \tag{A13}$$

Appendix B Calculate the gyrophase from particle positions

To obtain wave phase from equation (A3), we need to calculate $\cos(\phi')$, where ϕ' is 90° minus the gyrophase ϕ. The potion vector of an particle is

$$\mathbf{p} = \mathbf{e_x}p_x + \mathbf{e_y}p_y + \mathbf{e_z}p_z \ . \tag{B1}$$

The guiding center of the particle is given by

$$\mathbf{R_{gc}} = \mathbf{p} + r_L\hat{a} \ , \tag{B2}$$

where $\hat{a}$ is the direction from the particle to the guiding center given by

$$\hat{a} = \frac{\mathbf{B_0}\times\mathbf{v}_\perp}{|\mathbf{B_0}\times\mathbf{v}_\perp|} \ , \tag{B3}$$

and the parallel velocity vector $\mathbf{v}_\parallel$ and the perpendicular velocity vector $\mathbf{v}_\perp$ of the particle are given by

$$\mathbf{v}_\parallel = \frac{\mathbf{v}\cdot\mathbf{B_0}}{|\mathbf{B_0}|^2}\mathbf{B_0} \ , \tag{B4}$$

$$\mathbf{v}_\perp = \mathbf{v} - \mathbf{v}_\parallel \,. \tag{B5}$$

The $\mathbf{e}_{\mathbf{x}''}$ is written as

$$\mathbf{e}_{\mathbf{x}''} = \frac{\mathbf{B_0} \times (\mathbf{R_{gc}} \times \mathbf{B_0})}{|\mathbf{B_0} \times (\mathbf{R_{gc}} \times \mathbf{B_0})|} \,. \tag{B6}$$

Finally, we obtain $\cos(\phi')$ by

$$\cos(\phi') = -\hat{a} \cdot \mathbf{e}_{\mathbf{x}''} \,. \tag{B7}$$

Acknowledgments

The simulation data used in this paper are obtained from numerical integration of equation (1) in Kubota and Omura (2018) by the Buneman-Boris method. The computer simulation was performed on the A-KDK computer system at Research Institute for Sustainable Humanosphere, Kyoto University. Simulation code and data are accessible at repository http://doi.org/10.5281/zenodo.4773988. This work was supported by MEXT/JSPS KAKENHI Grants 17H06140.

References

Abel, B., & Thorne, R. M. (1998). Electron scattering loss in earth's inner magnetosphere: 1. dominant physical processes. *Journal of Geophysical Research: Space Physics*, *103*(A2), 2385–2396.

Anderson, K., & Milton, D. (1964). Balloon observations of x rays in the auroral zone: 3. high time resolution studies. *Journal of Geophysical Research*, *69*(21), 4457–4479.

Baker, D., Fritz, T., Wilken, B., Higbie, P., Kaye, S., Kivelson, M., ... others (1982). Observation and modeling of energetic particles at synchronous orbit on july 29, 1977. *Journal of Geophysical Research: Space Physics*, *87*(A8), 5917–5932.

Bortnik, J., & Thorne, R. (2007). The dual role of elf/vlf chorus waves in the acceleration and precipitation of radiation belt electrons. *Journal of Atmospheric and Solar-Terrestrial Physics*, *69*(3), 378–386.

Breneman, A., Crew, A., Sample, J., Klumpar, D., Johnson, A., Agapitov, O., ... others (2017). Observations directly linking relativistic electron microbursts to whistler mode chorus: Van allen probes and firebird ii. *Geophysical Research Letters*, *44*(22), 11–265.

Chen, L., Breneman, A. W., Xia, Z., & Zhang, X.-j. (2020). Modeling of bouncing electron microbursts induced by ducted chorus waves. *Geophysical Research Letters*, *47*(17), e2020GL089400.

Hikishima, M., Omura, Y., & Summers, D. (2010). Microburst precipitation of energetic electrons associated with chorus wave generation. *Geophysical Research Letters*, *37*(7).

Hiraga, R., & Omura, Y. (2020). Acceleration mechanism of radiation belt electrons through interaction with multi-subpacket chorus waves. *Earth, Planets and Space*, *72*(1), 1–14.

Horne, R., & Thorne, R. (2003). Relativistic electron acceleration and precipitation during resonant interactions with whistler-mode chorus. *Geophysical research letters*, *30*(10).

Hsieh, Y.-K., Kubota, Y., & Omura, Y. (2020). Nonlinear evolution of radiation belt electron fluxes interacting with oblique whistler mode chorus emissions. *Journal of Geophysical Research: Space Physics*, *125*(2), e2019JA027465.

Hsieh, Y.-K., & Omura, Y. (2017a). Nonlinear dynamics of electrons interacting with oblique whistler mode chorus in the magnetosphere. *Journal of Geophysical Research: Space Physics*, *122*(1), 675–694.

Hsieh, Y.-K., & Omura, Y. (2017b). Study of wave-particle interactions for whistler mode waves at oblique angles by utilizing the gyroaveraging method. *Radio Science*, *52*, 1268–1281. doi: 10.1002/2017RS006245

Kasahara, S., Miyoshi, Y., Yokota, S., Mitani, T., Kasahara, Y., Matsuda, S., ... others (2018). Pulsating aurora from electron scattering by chorus waves. *Nature*, *554*(7692), 337–340.

Kennel, C. F., & Petschek, H. (1966). Limit on stably trapped particle fluxes. *Journal of Geophysical Research*, *71*(1), 1–28.

Kersten, K., Cattell, C., Breneman, A., Goetz, K., Kellogg, P., Wygant, J., ... Roth, I. (2011). Observation of relativistic electron microbursts in conjunction with intense radiation belt whistler-mode waves. *Geophysical Research Letters*, *38*(8).

Kubota, Y., & Omura, Y. (2018). Nonlinear dynamics of radiation belt electrons interacting with chorus emissions localized in longitude. *Journal of Geophysical Research: Space Physics*, *123*(6), 4835–4857.

Kurita, S., Miyoshi, Y., Blake, J. B., Reeves, G. D., & Kletzing, C. A. (2016). Relativistic electron microbursts and variations in trapped mev electron fluxes during the 8–9 october 2012 storm: Sampex and van allen probes observations. *Geophysical Research Letters*, *43*(7), 3017–3025.

Lakhina, G., Tsurutani, B., Verkhoglyadova, O., & Pickett, J. (2010). Pitch angle transport of electrons due to cyclotron interactions with the coherent chorus subelements. *Journal of Geophysical Research: Space Physics*, *115*(A8).

Li, W., Thorne, R., Angelopoulos, V., Bortnik, J., Cully, C. M., Ni, B., ... Magnes, W. (2009). Global distribution of whistler-mode chorus waves observed on the themis spacecraft. *Geophysical Research Letters*, *36*(9).

Li, X., Baker, D., Temerin, M., Reeves, G., & Belian, R. (1998). Simulation of dispersionless injections and drift echoes of energetic electrons associated with substorms. *Geophysical Research Letters*, *25*(20), 3763–3766.

Meredith, N. P., Horne, R. B., Thorne, R. M., & Anderson, R. R. (2003). Favored regions for chorus-driven electron acceleration to relativistic energies in the earth's outer radiation belt. *Geophysical Research Letters*, *30*(16).

Millan, R., & Baker, D. (2012). Acceleration of particles to high energies in earth's radiation belts. *Space Science Reviews*, *173*(1), 103–131.

Miyoshi, Y., Katoh, Y., Nishiyama, T., Sakanoi, T., Asamura, K., & Hirahara, M. (2010). Time of flight analysis of pulsating aurora electrons, considering wave-particle interactions with propagating whistler mode waves. *Journal of Geophysical Research: Space Physics*, *115*(A10).

Miyoshi, Y., Oyama, S., Saito, S., Kurita, S., Fujiwara, H., Kataoka, R., ... others (2015). Energetic electron precipitation associated with pulsating aurora: Eiscat and van allen probe observations. *Journal of Geophysical Research: Space Physics*, *120*(4), 2754–2766.

Mourenas, D., Artemyev, A., Agapitov, O., Krasnoselskikh, V., & Mozer, F. (2015). Very oblique whistler generation by low-energy electron streams. *Journal of Geophysical Research: Space Physics*, *120*(5), 3665–3683.

Mozer, F., Agapitov, O., Blake, J., & Vasko, I. (2018). Simultaneous observations of lower band chorus emissions at the equator and microburst precipitating electrons in the ionosphere. *Geophysical Research Letters*, *45*(2), 511–516.

Nakamura, R., Baker, D., Blake, J., Kanekal, S., Klecker, B., & Hovestadt, D. (1995). Relativistic electron precipitation enhancements near the outer edge of the radiation belt. *Geophysical research letters*, *22*(9), 1129–1132.

Nakamura, R., Isowa, M., Kamide, Y., Baker, D., Blake, J., & Looper, M. (2000). Sampex observations of precipitation bursts in the outer radiation belt. *Journal of Geophysical Research: Space Physics*, *105*(A7), 15875–15885.

Nakamura, S., Omura, Y., Kletzing, C., & Baker, D. (2019). Rapid precipitation of relativistic electron by emic rising-tone emissions observed by the van allen

probes. *Journal of Geophysical Research: Space Physics*, *124*(8), 6701–6714.

Nishimura, Y., Bortnik, J., Li, W., Thorne, R. M., Lyons, L. R., Angelopoulos, V., ... others (2010). Identifying the driver of pulsating aurora. *science*, *330*(6000), 81–84.

Omura, Y. (2021). Nonlinear wave growth theory of whistler-mode chorus and hiss emissions in the magnetosphere. *Earth, Planets and Space*, *73*(1), 1–28.

Omura, Y., Hikishima, M., Katoh, Y., Summers, D., & Yagitani, S. (2009). Nonlinear mechanisms of lower-band and upper-band vlf chorus emissions in the magnetosphere. *Journal of Geophysical Research: Space Physics*, *114*(A7).

Omura, Y., Hsieh, Y.-K., Foster, J. C., Erickson, P. J., Kletzing, C. A., & Baker, D. N. (2019). Cyclotron acceleration of relativistic electrons through landau resonance with obliquely propagating whistler-mode chorus emissions. *Journal of Geophysical Research: Space Physics*, *124*(4), 2795–2810.

Omura, Y., Katoh, Y., & Summers, D. (2008). Theory and simulation of the generation of whistler-mode chorus. *Journal of Geophysical Research: Space Physics*, *113*(A4).

Omura, Y., Miyashita, Y., Yoshikawa, M., Summers, D., Hikishima, M., Ebihara, Y., & Kubota, Y. (2015). Formation process of relativistic electron flux through interaction with chorus emissions in the earth's inner magnetosphere. *Journal of Geophysical Research: Space Physics*, *120*(11), 9545–9562.

Omura, Y., & Summers, D. (2006). Dynamics of high-energy electrons interacting with whistler mode chorus emissions in the magnetosphere. *Journal of Geophysical Research: Space Physics*, *111*(A9).

Reeves, G., Fritz, T., Cayton, T., & Belian, R. (1990). Multi-satellite measurements of the substorm injection region. *Geophysical Research Letters*, *17*(11), 2015–2018.

Rosenberg, T., Wei, R., Detrick, D., & Inan, U. (1990). Observations and modeling of wave-induced microburst electron precipitation. *Journal of Geophysical Research: Space Physics*, *95*(A5), 6467–6475.

Saito, S., Miyoshi, Y., & Seki, K. (2012). Relativistic electron microbursts associated with whistler chorus rising tone elements: Gemsis-rbw simulations. *Journal of Geophysical Research: Space Physics*, *117*(A10).

Santolík, O., Gurnett, D., Pickett, J., Chum, J., & Cornilleau-Wehrlin, N. (2009). Oblique propagation of whistler mode waves in the chorus source region. *Journal of Geophysical Research: Space Physics*, *114*(A12).

Summers, D., Ni, B., & Meredith, N. P. (2007). Timescales for radiation belt electron acceleration and loss due to resonant wave-particle interactions: 2. evaluation for vlf chorus, elf hiss, and electromagnetic ion cyclotron waves. *Journal of Geophysical Research: Space Physics*, *112*(A4).

Summers, D., Thorne, R. M., & Xiao, F. (1998). Relativistic theory of wave-particle resonant diffusion with application to electron acceleration in the magnetosphere. *Journal of Geophysical Research: Space Physics*, *103*(A9), 20487–20500.

Thorne, R. M., O'Brien, T., Shprits, Y., Summers, D., & Horne, R. B. (2005). Timescale for mev electron microburst loss during geomagnetic storms. *Journal of Geophysical Research: Space Physics*, *110*(A9).

Tsurutani, B. T., Lakhina, G. S., & Verkhoglyadova, O. P. (2013). Energetic electron (¿ 10 kev) microburst precipitation,˜ 5–15 s x-ray pulsations, chorus, and wave-particle interactions: A review. *Journal of Geophysical Research: Space Physics*, *118*(5), 2296–2312.

Tsurutani, B. T., Verkhoglyadova, O. P., Lakhina, G. S., & Yagitani, S. (2009). Properties of dayside outer zone chorus during hildcaa events: Loss of energetic electrons. *Journal of Geophysical Research: Space Physics*, *114*(A3).

Turner, D. L., Fennell, J., Blake, J., Claudepierre, S., Clemmons, J., Jaynes, A., ... others (2017). Multipoint observations of energetic particle injections and

703 substorm activity during a conjunction between magnetospheric multiscale
704 (mms) and van allen probes. *Journal of Geophysical Research: Space Physics*,
705 *122*(11), 11–481.
706 Yamaguchi, K., Matsumuro, T., Omura, Y., & Nunn, D. (2013). Ray tracing of
707 whistler-mode chorus elements: implications for generation mechanisms of ris-
708 ing and falling tone emissions. In *Annales geophysicae* (Vol. 31, pp. 665–673).